



ATATURK
UNIVERSITY
PUBLICATIONS

Journal of Anatolian Physics and Astronomy

Official Journal of Atatürk University Faculty of Science

Volume 3 Issue 1 June 2024

EISSN 2791-8718
<https://dergipark.org.tr/en/pub/japa>

Journal of Anatolian Physics and Astronomy

CHIEF EDITOR / BAŐ EDITÖR

Erdem ŐAKAR 

Science Faculty, Department of Physics,
Atatürk University, Erzurum, Turkey
*Fen Fakóltesi, Fizik Bölümü, Atatürk
Üniversitesi, Erzurum, Türkiye*

ASSOCIATE EDITORS / YARDIMCI EDITÖRLER

Yakup KURUCU 

Science Faculty, Department of Physics,
Atatürk University, Erzurum, Turkey
*Fen Fakóltesi, Fizik Bölümü, Atatürk
Üniversitesi, Erzurum, Türkiye*

Bekir GÖRBULAK 

Science Faculty, Department of Physics,
Atatürk University, Erzurum, Turkey
*Fen Fakóltesi, Fizik Bölümü, Atatürk
Üniversitesi, Erzurum, Türkiye*

Ganim GEÇİM 

Science Faculty, Department of Astronomy
and Astrophysics, Atatürk University,
Erzurum, Turkey
*Fen Fakóltesi, Astronomi ve Astrofizik
Bölümü, Atatürk Üniversitesi, Erzurum,
Türkiye*

Elif DAŐ 

Science Faculty, Department of Physics,
Atatürk University, Erzurum, Turkey
*Fen Fakóltesi, Fizik Bölümü, Atatürk
Üniversitesi, Erzurum, Türkiye*

Melek FIDAN 

Science Faculty, Department of Physics,
Atatürk University, Erzurum, Turkey
*Fen Fakóltesi, Fizik Bölümü, Atatürk
Üniversitesi, Erzurum, Türkiye*

Aykut ÖZDÖNMEZ 

Science Faculty, Department of Astronomy
and Astrophysics, Atatürk University,
Erzurum, Turkey
*Fen Fakóltesi, Astronomi ve Astrofizik
Bölümü, Atatürk Üniversitesi, Erzurum,
Türkiye*

ADVISORY BOARD / DANIŐMA KURULU

Ali GÖROL

Science Faculty, Department of Physics,
Atatürk University, Erzurum, Turkey
*Fen Fakóltesi, Fizik Bölümü, Atatürk
Üniversitesi, Erzurum, Türkiye*

Emre GÖR

Department of Turkish Language and
Literature, Gazi University, Ankara, Turkey
*Gazi Üniversitesi, Türk Dili ve Edebiyatı
Bölümü, Ankara, Türkiye*

Mehmet ERTUĞRUL

Department of Turkish Language and
Literature, Fırat University, Elazığ, Turkey
*Fırat Üniversitesi, Türk Dili ve Edebiyatı
Bölümü, Elazığ, Türkiye*

Orhan İÇELLİ

Department of Turkish Language and
Literature, Trakya University, Trakya, Turkey
*Trakya Üniversitesi, Türk Dili ve Edebiyatı
Bölümü, Edirne, Türkiye*

Cahit YEŐİLYAPRAK

Department of History, Yeditepe University,
Turkey
*Yeditepe Üniversitesi, Tarih Bölümü, İstanbul,
Türkiye*

Lorent JOLISSAINT

Department of Social Sciences and Turkish
Education, Yıldız Technical University,
İstanbul, Turkey
*Yıldız Teknik Üniversitesi, Sosyal Bilimler ve
Türkçe Eğitimi Bölümü, İstanbul, Türkiye*

FOREIGN LANGUAGE CONSULTANTS /

YABANCI DİL DANIŐMANLARI

Erdinç ÖZ

Science Faculty, Department of Physics,
Atatürk University, Erzurum, Turkey
*Fen Fakóltesi, Fizik Bölümü, Atatürk
Üniversitesi, Erzurum, Türkiye*

Aykut ÖZDÖNMEZ

Science Faculty, Department of Astronomy
and Astrophysics, Atatürk University,
Erzurum, Turkey
*Fen Fakóltesi, Astronomi ve Astrofizik
Bölümü, Atatürk Üniversitesi, Erzurum,
Türkiye*

Elif DAŐ

Science Faculty, Department of Physics,
Atatürk University, Erzurum, Turkey
*Fen Fakóltesi, Fizik Bölümü, Atatürk
Üniversitesi, Erzurum, Türkiye*

AyŐenur ÖZTÖRK AYDIN

Engineering Faculty, Department of Chemical
Engineering, Atatürk University, Erzurum,
Turkey
*Mühendislik Fakóltesi, Kimya Mühendisliđi
Bölümü, Atatürk Üniversitesi, Erzurum,
Türkiye*

Journal of Anatolian Physics and Astronomy

About the Journal of Anatolian Physics and Astronomy

Journal of Anatolian Physics and Astronomy is a peer-reviewed, open-access, online-only journal published by Atatürk University.

The journal is published biannual in both Turkish, and English, with articles released in June, and December.

Abstracting and Indexing

Journal of Anatolian Physics and Astronomy is covered in the following abstracting and indexing databases;

- EBSCO

Aims

Journal of Anatolian Physics and Astronomy aims to contribute to the literature by publishing manuscripts at the highest scientific level in physics and astronomy. The journal publishes original articles, and reviews that are prepared in accordance with ethical guidelines.

Scope and Audience

The scope of the journal includes but not limited to relevant to the topics of atomic and molecular physics, condensed matter physics, nuclear physics, particle, physics, quantum physics, optical physics, biophysics, thermodynamics, astrophysics, astronomical techniques and methods, galaxies, gravitation and cosmology, planets, comets, solar and stellar physics, space and all other related interdisciplinary theoretical researches.

The target audience of the journal includes researchers and specialists who are interested or working in all fields in the journal's scope.

Disclaimer

Statements or opinions expressed in the manuscripts published in the journal reflect the views of the author(s) and not the opinions of the editors, editorial board, and/or publisher; the editors, editorial board, and publisher disclaim any responsibility or liability for such materials.

Open Access Statement

Journal of Anatolian Physics and Astronomy is an open access publication. Starting on June 2024, all content published in the journal is licensed under the Creative Commons Attribution-NonCommercial (CC BY-NC) 4.0 International License which allows third parties to use the content for non-commercial purposes as long as they give credit to the original work. This license allows for the content to be shared and adapted for non-commercial purposes, promoting the dissemination and use of the research published in the journal. All published content is available online, free of charge at <https://dergipark.org.tr/en/pub/japa>. When using previously published content, including figures, tables, or any other material in both print and electronic formats, authors must obtain permission from the copyright holder. Legal, financial and criminal liabilities in this regard belong to the author(s).

You can find the current version of the Instructions to Authors at <https://dergipark.org.tr/en/pub/japa/writing-rules>



Contact (Editor in Chief) / İletişim (Baş Editör)

Erdem ŞAKAR

Science Faculty, Department of Physics,
Atatürk University, Erzurum, Turkey
*Fen Fakültesi, Fizik Bölümü, Atatürk Üniversitesi,
Erzurum, Türkiye*

✉ erdem@atauni.edu.tr

✉ japa@atauni.edu.tr

🌐 <https://dergipark.org.tr/en/pub/japa>

☎ +90 442 231 41 72

Contact (Publisher) / İletişim (Yayıncı)

Atatürk University

Atatürk University, Erzurum, Turkey
Atatürk Üniversitesi Rektörlüğü 25240 Erzurum, Türkiye

✉ ataunijournals@atauni.edu.tr

🌐 <https://bilimseldergiler.atauni.edu.tr>

☎ +90 442 231 15 16

Journal of Anatolian Physics and Astronomy

Journal of Anatolian Physics and Astronomy Hakkında

Journal of Anatolian Physics and Astronomy, Atatürk Üniversitesi tarafından yayınlanan hakemli, açık erişimli, yalnızca çevrimiçi bir dergidir.

Dergi, Haziran ve Aralık aylarında olmak üzere Türkçe ve İngilizce olarak yılda iki kez yayınlanmaktadır.

Özetleme ve İndeksleme

Journal of Anatolian Physics and Astronomy aşağıdaki özetleme ve indeksleme veri tabanlarında yer almaktadır:

- EBSCO

Amaç

Journal of Anatolian Physics and Astronomy, fizik ve astronomi alanında en yüksek bilimsel düzeyde makaleler yayınlayarak literatüre katkıda bulunmayı amaçlamaktadır. Dergide etik kurallara uygun olarak hazırlanmış özgün makaleler ve derlemeler yayınlanmaktadır.

Kapsam ve Hedef Kitle

Derginin kapsamına atom ve moleküler fizik, yoğun madde fiziği, nükleer fizik, parçacık fizik, kuantum fiziği, optik fizik, biyofizik, termodinamik, astrofizik, astronomik teknik ve yöntemler, galaksiler, galaksiler, yerçekimi ve kozmoloji, gezegenler, kuyruklu yıldızlar, güneş ve yıldız fiziği, uzay ve ilgili tüm disiplinler arası teorik araştırmalar girmektedir.

Derginin hedef kitle, derginin kapsamına giren tüm alanlarla ilgilenen veya çalışan araştırmacı ve uzmanları içermektedir.

Sorumluluk Reddi

Dergide yayınlanan yazılarda ifade edilen ifadeler veya görüşler, editörlerin, yayın kurulunun ve/veya yayıncının görüşlerini değil, yazar(lar)ın görüşlerini yansıtır; editörler, yayın kurulu ve yayıncı bu tür materyaller için herhangi bir sorumluluk veya yükümlülük kabul etmemektedir.

Açık Erişim Bildirimi

Journal of Anatolian Physics and Astronomy açık erişimli bir dergidir. 2024 Haziran ayından itibaren dergide yayınlanan tüm içerik, Creative Commons Attribution-NonCommercial (CC BY-NC) 4.0 International License lisansı ile yayınlanmaktadır. Bu lisans, içeriğin ticari olmayan amaçlarla paylaşılmasını ve adapte edilmesini sağlayarak dergide yayınlanan araştırmaların yayılmasını ve kullanılmasını teşvik eder. Haziran 2024'ten önce yayınlanan içerik, geleneksel telif hakkı kapsamında lisanslanmıştır ancak arşiv ücretsiz olarak hâlâ erişime açıktır. Tüm yayımlanan içerikler <https://dergipark.org.tr/tr/pub/japa> adresinden çevrimiçi olarak ücretsiz olarak erişilebilir. Daha önce yayınlanmış içeriği, figürleri, tabloları veya diğer herhangi bir materyali basılı veya elektronik formatta kullanırken yazarlar, telif hakkı sahibinden izin almakla sorumludur. Bu konuda yasal, mali ve cezai sorumluluklar yazar(lara) aittir.

Yazarlara Bilgi'nin güncel versiyonuna <https://dergipark.org.tr/tr/pub/japa/writing-rules> adresinden ulaşabilirsiniz.



Contact (Editor in Chief) / İletişim (Baş Editör)

Erdem ŞAKAR

Science Faculty, Department of Physics,
Atatürk University, Erzurum, Turkey
Fen Fakültesi, Fizik Bölümü, Atatürk Üniversitesi,
Erzurum, Türkiye

✉ erdem@atauni.edu.tr

✉ japa@atauni.edu.tr

🌐 <https://dergipark.org.tr/en/pub/japa>

☎ +90 442 231 41 72

Contact (Publisher) / İletişim (Yayıncı)

Atatürk University

Atatürk University, Erzurum, Turkey
Atatürk Üniversitesi Rektörlüğü 25240 Erzurum, Türkiye

✉ ataunijournals@atauni.edu.tr

🌐 <https://bilimseldergiler.atauni.edu.tr>

☎ +90 442 231 15 16

Journal of Anatolian Physics and Astronomy

CONTENTS / İÇİNDEKİLER

Research Articles/Araştırma Makaleleri

- 1** **Rayleigh Şaçılma Üzerine Deneysel Bir Çalışma**
An Experimental Study on Rayleigh Scattering
Salih Z. ERZENEÖĞLU

- 7** **Aynı Koşullar Altında Üretilen Au/p-TlInS₂/n-InP Pseudo Schottky Eklemlerin Karakteristik Parametrelerinin İstatistiksel İncelenmesi**
Statistical Investigation of Characteristic Parameters for Au/p-TlInS₂/n-InP Pseudo Schottky Junctions Produced Under the Same Conditions
Seda YAZICI, Fatih AKTAŞ, Ayşe Nida BEŞTAŞ, Nezaket KULAKAÇ, Dilek ASLANCAN, Bahattin ABAY

- 19** **Kozmik Işınlr ve Toplam Bulut Örtüsü Arasındaki İlişkinin LSTM Ağlarıyla Analizi**
Analyzing the Relationship Between Cosmic Rays and Total Cloud Cover with LSTM Networks
Ahmet POLATOĞLU

- 27** **Gama Radyasyonun Amitriptyline Hydrochloride Üzerinde Oluşturduğu Yapısal Bozuklukların Elektron Paramanyetik Rezonans (EPR) ve Simülasyon Tekniği ile İncelenmesi**
Analysis of Structural Defects Caused by Gamma Radiation on Amitriptyline Hydrochloride Through Electron Paramagnetic Resonance (EPR) and Simulation Technique
Firat AKBALIK

- 36** **Bridgman/Stockbarger Tekniği Kullanılarak Büyütülen XIn₂Se₄ Üçlü Yarı İletkenlerin Teorik Yapısal Karakterizasyonu**
Theoretical Structural Characterization of XIn₂Se₄ Ternary Semiconductors Wanted to be Grow Using the Bridgman/Stockbarger Technique
Bekir GÜRBULAK

An Experimental Study on Rayleigh Scattering

Rayleigh Şaçılma Üzerine Deneysel Bir Çalışma

Abstract

The Rayleigh scattering cross-sections were determined in the region of $22 \leq Z \leq 82$ at 126° using an energy dispersive X-ray fluorescence spectrometer at 59.5 keV energy and a Si(Li) detector. This paper presents and discusses the results of this study. The predictions of several form factor theories were compared with experimental Rayleigh scattering differential cross-sections

Keywords: Rayleigh scattering, Differential cross section, X-ray fluorescence spectrometer

Öz

Bu çalışmada, Rayleigh saçılma diferansiyel tesir kesitleri enerji ayrımlı X-ışını flöresans spektrometreyle $22 \leq Z \leq 82$ bölgesinde 126° lik saçılma açısında ölçüldü. Deneyde 59.5 keV enerjili fotonlar ve bir Si(Li) dedektörü kullanıldı. Sonuçlar bu makalede sunuldu ve tartışıldı. Deneysel Rayleigh saçılma diferansiyel tesir kesitleri farklı form faktör teorilerinin sonuçlarıyla karşılaştırıldı.

Anahtar Kelimeler: Rayleigh saçılma, Diferansiyel tesir kesiti, X-ışını flöresans spektrometre

Salih Z. ERZENEÖĞLU 
Atatürk University, Department of Physics,
Faculty of Sciences, Erzurum, Turkey



Corresponding Author/ Sorumlu Yazar:
Salih Z. ERZENEÖĞLU
E-mail: salih@atauni.edu.tr

Received/ Geliş Tarihi 02.05.2024
Accepted/Kabul Tarihi 04.06.2024
Publication Date/
Yayın Tarihi 27.06.2024

Cite this article

Erzeneoglu, S. Z. (2024) An Experimental Study on Rayleigh Scattering. *Journal of Anatolian Physics and Astronomy*, 3(1), 1-6.



Content of this journal is licensed under a Creative Commons Attribution-Noncommercial 4.0 International License.

Introduction

Rayleigh scattering studies play a major role in fundamental atomic-physics research. For this reason, there has been much research in the literature. For the liver, kidney, muscle, and fat, Böke (2014) calculated coherent and incoherent scattering, photoelectric cross-sections, and linear attenuation coefficients. Thulasi et al. (2021) experimentally calculated the angle integrated total scattering cross sections of a few rare earth oxides for 59.54 keV gamma rays in the angular ranges of 0-40, 0-60, 0-80, and 0-100. They examined how the effective atomic number of the chosen compounds varied in relation to the angle-integrated coherent scattering cross-section. Angle-integrated coherent scattering cross-sections of a few components at modest momentum transfers throughout four angular ranges were published by (Vinaykumar & Umesh, 2016). The coherent (Rayleigh) to incoherent (Compton) scattering cross-section ratio of elements in the range $6 \leq Z \leq 82$ was experimentally established for 145 keV incident gamma photons by Singh et al. (2013). They were found to be in agreement with theoretical predictions based on the non-relativistic form factor, relativistic form factor, modified form factor, and S-matrix theory, which correspond to 4.939, 6.704, and 8.264 \AA^{-1} photon momentum transfer. At an energy of 59.54 keV, Thanh et al. (2020) used six well-known techniques to obtain experimental data of the Rayleigh to Compton scattering ratios depending on the effective atomic number of the 15 powder samples in the range $10 < Z < 30$. They fitted the Rayleigh peak using a Gaussian function using Root software and the Compton peak using a Voigt function using a new fitting process with the least squares method. Utilizing a Ge(Li) detector, İçelli and Erzeneoğlu (2002) determined differential cross-sections for coherent and Compton scattering of 59.5 keV gamma-rays at scattering 55° and 115° . Theoretical coherent and Compton scattering differential cross-sections were measured by interpolating atomic form factors and incoherent scattering functions corresponding to 2.216 and 4.048 \AA^{-1} photon momentum transfer. Rayleigh scattering cross section measurements for 39.5 keV (Sm-K α_2), 40.1 keV (Sm-K α_1), and 45.4 keV (Sm-K $\beta_{1,3}$) X-ray photons in 35 elements with $26 \leq Z \leq 83$ at a backward angle of 139° have been reported by Upmanyu et al. (2017). They carried out scattering experiments using a secondary photon source made up of a samarium (62Sm) target energized by 59.54 keV gamma-rays from the Am-241 radioactive source in a reflection-mode geometrical setup. To highlight the necessity of updating publicly accessible databases to incorporate the current atomic form factor tabulations, which allows the determination of a compound's linear differential scattering coefficient from a weighted sum of its elemental components. Tartari et al. (2005) have provided new small angle coherent scattering data. These data take into account the impact of the large-scale sample structure arrangement in addition to the molecular interference effect. Volotka et al. (2016) study theorize the Rayleigh scattering of X-rays by highly charged ions with numerous electrons. Beyond the independent-particle approximation (IPA), which is typically used to describe Rayleigh scattering, researchers have investigated many electron effects. Del Lama et al. (2015) have employed the Rayleigh to Compton scattering ratio (R/C) as a trustworthy quantitative technique for materials analysis, particularly biological ones. Their goal was to apply the R/C approach to determine which phantom was best suited to simulate biological tissues while taking into account two distinct experimental scenarios: scattering and attenuation. In the present study, Rayleigh scattering cross sections were reported for 14 elements.

Theoretical Basis

The differential cross-section for Rayleigh scattering of γ -rays by a target atom is obtained using the equation (Kane et al., 1983)

$$\frac{n}{n^{Al}} = \frac{T}{T^{Al}} \frac{N}{N^{Al}} \frac{\varepsilon}{\varepsilon^c} \left[\frac{d\sigma_{Al}}{d\Omega} \right]^{-1} \frac{d\sigma}{d\Omega} \quad (1)$$

where n is the number of photons Rayleigh scattered, n^{Al} is the number of photons Compton scattered from Al, T^{Al} and T are, respectively, the transmission factors for Al at the Compton energy and for 59.5 keV energy with the target, N^{Al} and N are the number of scattering atoms in Al and the scatterer, ε^c and ε are, respectively, the detector photopeak efficiencies for Compton and Rayleigh scattered γ -rays,

$$\frac{d\sigma_{Al}}{d\Omega} = \frac{d\sigma^{KN}}{d\Omega} S(x, Z) \quad (2)$$

is the Compton scattering cross-section for the aluminum, $d\sigma^{KN}/d\Omega$ is the Klein–Nishina cross-section per electron,

$S(x, Z)$ is the incoherent scattering function, x is the photon momentum transfer [$x = \sin(\theta/2)/\lambda$] \AA^{-1} , θ is the angle of scattering, λ is the wavelength of the incident radiation in Angstrom, Z is the atomic number of the scattering atom.

The theoretical Rayleigh scattering differential cross-section is calculated by using

$$\frac{d\sigma}{d\Omega} = \frac{1}{2} r_e^2 (1 + \cos^2\theta) [F(x, Z)]^2 \quad (3)$$

where r_e is the classical electron radius ($2.8179380 \times 10^{-15} \text{ m}$), $F(x, Z)$ is the atomic form factor.

Experimental Basis

The experimental setup used is given in Figure. 1. In this study, we used a point source of Am-241 with an intensity of 100 mCi which emits 59.5 keV gamma rays. The source was placed in lead blocks to collimate rays. We used a Si(Li) detector having 4 mm in active diameter and 3 mm in sensitive crystal depth. The resolution of the detector was 160 eV at 5.9 keV energy. Measurements were taken under the same experimental conditions for 10800 s. The spectra were recorded using a 1024 channel analyser. To obtain the net pulse height spectra of the scattered γ -rays, a background spectrum without the scatterer was stripped from the spectrum acquired for an equal period of time under experimental conditions. High-purity elemental powders of Ti, Ni, Zn, Se, Mo, Ru, Yb, Gd, Dy, W, and Pb (purity > 99.9%), and Cd, Sn, and Te (purity > 99.5%) were used as scatterers. The thicknesses of the powder elements ranged from 0.018 to 0.050 g/cm². The target detector and target source distances were set to 5 cm, and the targets had an area of $25\pi \text{ mm}^2$. The scattering angle was 126° during the experiment. Particle size correction was performed using the following equation:

$$P = \frac{1 - \exp(-\mu d)}{\mu d} \quad (4)$$

where μ is the linear absorption coefficient (cm^{-1}) and d is the particle size (cm).

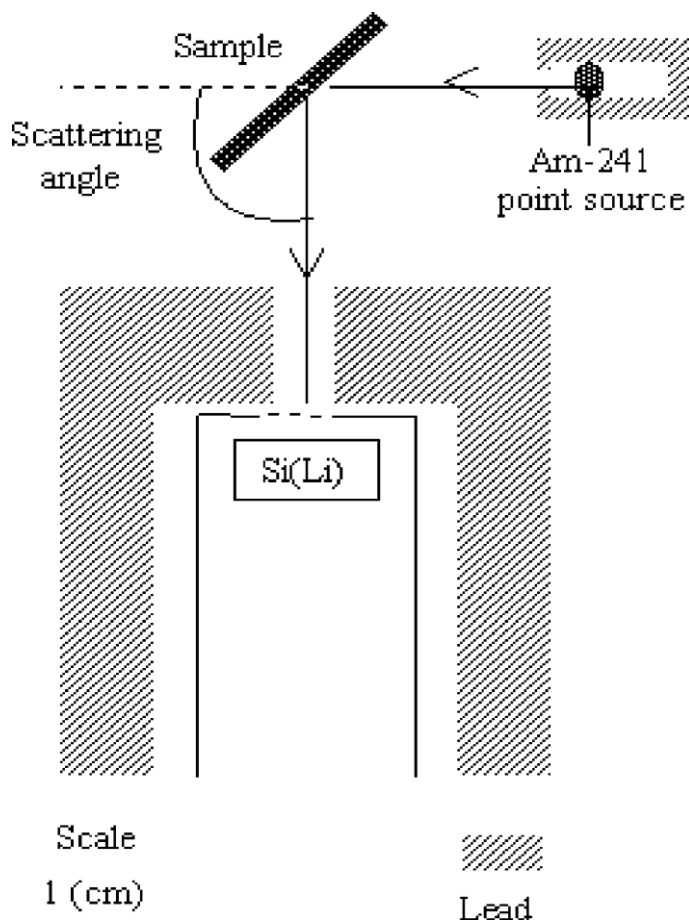


Figure 1. The experimental setup

Results and Discussion

The purpose of this research is to measure the Rayleigh scattering differential cross-sections of various materials. Table 1 displays the differential cross-sectional results for Rayleigh scattering, both theoretically and experimentally. Additionally, Fig. 2 presents a graphical comparison of the experimental data with the predictions of the nonrelativistic (NRFF) (Hubbell et al., 1975), relativistic (RFF) (Hubbell & O/Verbo, 1979), and relativistic modified form factor (RMFF) (Schaupp et al., 1983) theories. Differential scattering cross sections systematically increase with increasing atomic number, as shown in Fig. 2. It might be said that Rayleigh scattering becomes more prevalent as the atomic number rises since there are more electrons that are tightly bonded to nuclei. The contribution of Rayleigh is minimal for small-Z targets. The experimental results corresponded well with the predictions for all three formalisms in this region. The present experimental results, however, are smaller than the predictions of the NRFF and RFF theories, but are in good agreement with those of the RMFF theory in the high-Z zone. Furthermore, the findings highlight the significance of relativistic effects for high-Z components. Furthermore, the validity range of the form factor approximation for the bound electron description of elastic photon scattering is constrained (Kissel et al., 1980). In the total-atom form factor, the K shell predominates at bigger angles for this energy. Since L and higher shells become more significant and the form factor at this energy more precisely predicts these higher shells, the agreement between the experiment and predictions improves at smaller angles. For high-Z elements, the experimental results deviate from the theory, confirming the importance of electron-binding effects in the measurements. The experiment for Dy and Yb showed the largest difference between the predictions of the form factor approximation. This is because the K edges of these elements are closest to 59.9 keV (53.8 keV for Dy and 61.3 keV for Yb). Dispersion effects close to the K edges may be the cause of these anomalies. Previous studies have reported similar dispersion effects (Kissel et al., 1980), (Nayak et al., 1992). Less than 1.06% of the evaluations of the photopeak area were incorrect. The scattering angle precision is within $\pm 4\%$. The approximate estimate of inaccuracy in T was 2%.

Table 1. The experimental and theoretical differential cross sections (b/sr).

Element	Differential Cross section (b/sr)			
	Experimental	Theoretical		
		NRFF	RFF	RMFF
Ti	0.038	0.051	0.051	0.048
Ni	0.072	0.088	0.080	0.074
Zn	0.085	0.105	0.092	0.085
Se	0.110	0.149	0.128	0.117
Mo	0.258	0.299	0.280	0.251
Ru	0.315	0.350	0.338	0.303
Cd	0.433	0.463	0.478	0.425
Sn	0.522	0.525	0.556	0.493
Te	0.503	0.590	0.638	0.563
Gd	0.874	1.037	1.102	0.939
Dy	0.858	1.124	1.179	0.997
Yb	0.993	1.312	1.347	1.122
W	1.309	1.527	1.551	1.272
Pb	1.751	2.056	2.148	1.724

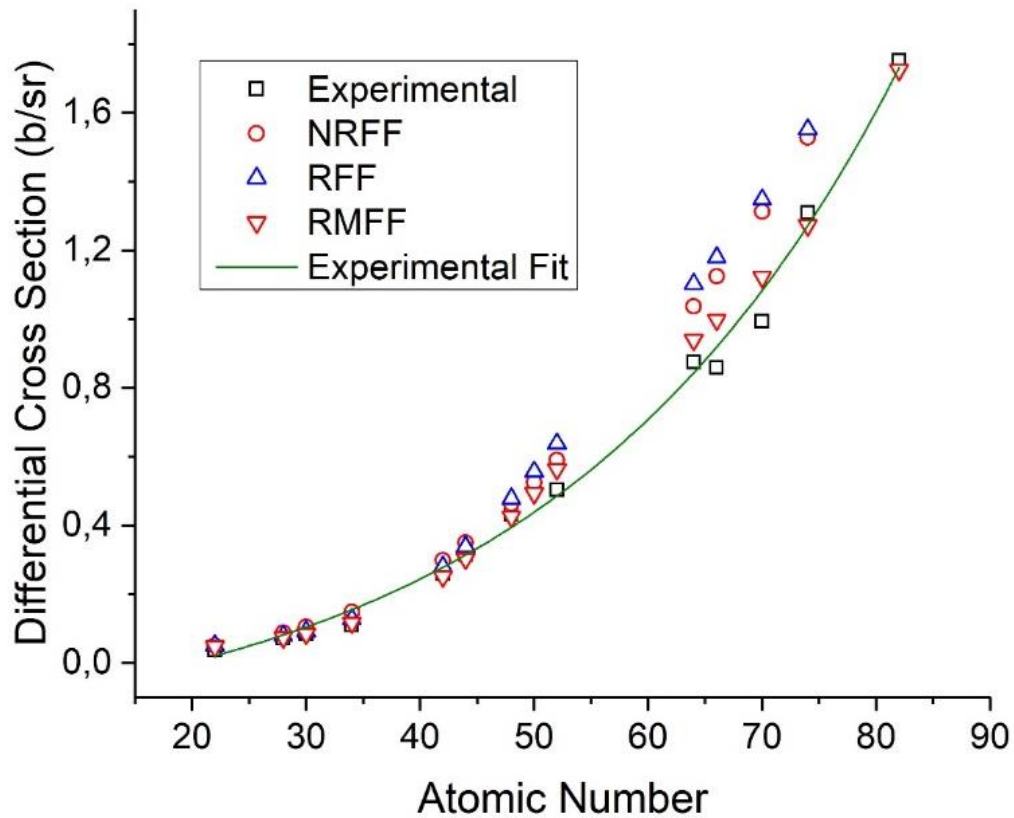


Figure 2. The differential cross section versus atomic number.

Conclusion

For photon energies of less than 2 MeV, elastic photon scattering is dominated by Rayleigh scattering and the contribution of bound atomic electrons to elastic photon scattering. Conversely, elastic scattering finds application in several experimental fields, including imaging, medical diagnostics, and material research. Among the mechanisms (photoeffect, scattering, and pair creation) principally responsible for attenuating thin beams of photons in matter is scattering, which plays a significant role in the energy range above the photoeffect L-edge but less than 10 MeV. I have provided precise values of the Rayleigh scattering differential cross sections for the elements Ti, Ni, Zn, Se, Mo, Ru, Cd, Sn, Te, Gd, Dy, Yb, W, and Pb in the current study. The current experimental study supports the superiority of the RMFF theory. In the future, similar research could be conducted using alternative approaches, energies, and scattering angles.

Peer-review: Externally peer-reviewed.

Conflict of Interest: The author has no conflicts of interest to declare.

Financial Disclosure: The author declared that this study has received no financial support.

Hakem Değerlendirmesi: Dış bağımsız.

Çıkar Çatışması: Yazar, çıkar çatışması olmadığını beyan etmiştir.

Finansal Destek: Yazar, bu çalışma için finansal destek almadığını beyan etmiştir.

References

- Böke, A. (2014). Linear attenuation coefficients of tissues from 1keV to 150keV. *Radiation Physics and Chemistry*, 102, 49–59. <https://doi.org/10.1016/j.radphyschem.2014.04.006>
- Del Lama, L., Soares, L., Antoniassi, M., & Poletti, M. (2015). Effective atomic numbers for materials of medical interest at low photon energy using the Rayleigh to Compton scattering ratio. *Nuclear Instruments and Methods in Physics Research. Section a, Accelerators, Spectrometers, Detectors and Associated Equipment/Nuclear Instruments & Methods in Physics Research. Section a, Accelerators, Spectrometers, Detectors and Associated Equipment*, 784, 597–601. <https://doi.org/10.1016/j.nima.2014.12.046>
- Hubbell, J. H., & O'Verbo, I. (1979). Relativistic atomic form factors and photon coherent scattering cross sections. *Journal of Physical and Chemical Reference Data*, 8(1), 69–106. <https://doi.org/10.1063/1.555593>
- Hubbell, J. H., Veigele, W. J., Briggs, E. A., Brown, R. T., Cromer, D. T., & Howerton, R. J. (1975). Atomic form factors, incoherent scattering functions, and photon scattering cross sections. *Journal of Physical and Chemical Reference Data*, 4(3), 471–538. <https://doi.org/10.1063/1.555523>
- İçelli, O., & Erzeneoğlu, S. (2002). Experimental study on ratios of coherent scattering to Compton scattering for elements with atomic numbers $26 \leq Z \leq 82$ in 59.5 keV for 55° and 115° . *Spectrochimica Acta. Part B, Atomic Spectroscopy*, 57(8), 1317–1323. [https://doi.org/10.1016/s0584-8547\(02\)00050-2](https://doi.org/10.1016/s0584-8547(02)00050-2)
- Kane, P. P., Mahajani, J., Basavaraju, G., & Priyadarsini, A. K. (1983). Scattering of 1.1732- and 1.3325-MeV gamma rays through small angles by carbon, aluminum, copper, tin, and lead. *Physical Review. A, General Physics*, 28(3), 1509–1516. <https://doi.org/10.1103/physreva.28.1509>
- Kissel, L., Pratt, R. H., & Roy, S. C. (1980). Rayleigh scattering by neutral atoms, 100 eV to 10 MeV. *Physical Review. A, General Physics*, 22(5), 1970–2004. <https://doi.org/10.1103/physreva.22.1970>
- Nayak, N. G., Siddappa, K., Balakrishna, K. M., & Lingappa, N. (1992). Coherent scattering of 59.5-keV γ rays by some medium and heavy elements. *Physical Review. A, Atomic, Molecular, and Optical Physics/Physical Review, a, Atomic, Molecular, and Optical Physics*, 45(7), 4490–4493. <https://doi.org/10.1103/physreva.45.4490>
- Schaupp, D., Schumacher, M., Smend, F., Rullhusen, P., & Hubbell, J. H. (1983). Small-Angle Rayleigh Scattering of Photons at High Energies: Tabulations of Relativistic HFS Modified Atomic Form Factors. *Journal of Physical and Chemical Reference Data*, 12(3), 467–512. <https://doi.org/10.1063/1.555690>
- Singh, M., Sharma, A., Singh, B., & Sandhu, B. (2013). An experimental study on cross-section ratio of coherent to incoherent scattering for 145 keV incident gamma photons. *Radiation Measurements*, 59, 30–36. <https://doi.org/10.1016/j.radmeas.2013.09.003>
- Tartari, A., Taibi, A., Bonifazzi, C., Gambaccini, M., & De Felici, M. (2005). Updating of x-ray coherent scattering cross-sections and their effects in microbeam and material analysis applications. *X-ray Spectrometry*, 34(5), 421–425. <https://doi.org/10.1002/xrs.847>
- Thanh, T. T., Minh, L. H., Cuong, N. Q. B., Chuong, H. D., Thong, N. D., Nguyen, V. H., Ho, P. L., Tai, C. T., & Van Tao, C. (2020). Study of different methods to estimate the Rayleigh to Compton scattering ratio and the effective atomic number ($10 < Z < 30$) using Si(Li) detector. *Nuclear Instruments and Methods in Physics Research. Section a, Accelerators, Spectrometers, Detectors and Associated Equipment/Nuclear Instruments & Methods in Physics Research. Section a, Accelerators, Spectrometers, Detectors and Associated Equipment*, 969, 163995. <https://doi.org/10.1016/j.nima.2020.163995>
- Thulasi, P. V., Joseph, A., Somashekarappa, H. M., & Kamat, V. A. (2021). Coherent Scattering Cross Sections of Some Rare Earth Compounds at Small Angles Below 10° for 59.54 KeV Gamma Rays. Social Science Research Network. <https://doi.org/10.2139/ssrn.3973501>
- Upmanyu, A., Singh, G., Duggal, H., Kainth, H., Bhalla, A., & Kumar, S. (2017). Measurement of large angle Rayleigh scattering cross sections for 39.5, 40.1 and 45.4 keV photons in elements with $26 \leq Z \leq 83$. *Applied Radiation and Isotopes*, 128, 125–131. <https://doi.org/10.1016/j.apradiso.2017.07.012>
- Vinaykumar, L., & Umesh, T. (2016). Small angle scattering of 59.54 keV photons by elemental samples in the atomic number region $13 \leq Z \leq 82$. *Journal of Radiation Research and Applied Sciences*, 9(1), 35–40. <https://doi.org/10.1016/j.jrras.2015.08.003>
- Volotka, A. V., Yerokhin, V. A., Surzhykov, A., Stöhlker, T., & Fritzsche, S. (2016). Many-electron effects on x-ray Rayleigh scattering by highly charged He-like ions. *Physical Review. A/Physical Review, A*, 93(2). <https://doi.org/10.1103/physreva.93.023418>

Statistical investigation of characteristic parameters for Au/p-TlInS₂/n-InP pseudo Schottky junctions produced under the same conditions

Aynı koşullar altında üretilen Au/p-TlInS₂/n-InP pseudo Schottky eklemlerin karakteristik parametrelerinin istatistiksel incelenmesi

Seda YAZICI¹ 

Fatih AKTAŞ¹ 

Ayşe Nida BEŞTAŞ¹ 

Nezaket KULAKAÇ¹ 

Dilek ASLANCAN¹ 

Bahattin ABAY^{2*} 

¹Atatürk University, Institute of Natural and Applied Sciences, Department of Physics, Erzurum, Turkey

²Atatürk University, Faculty of Science, Department of Physics, Erzurum, Turkey



*Sorumlu Yazar/Corresponding Author:

Bahattin Abay

E-mail: bahattinabay@yahoo.com

Geliş Tarihi/Received 10.05.2024

Kabul Tarihi/Accepted 05.06.2024

Yayın Tarihi/ 27.06.2024

Publication Date

Cite this article

Yazıcı, S. et al (2024). Statistical investigation of characteristic parameters for Au/p-TlInS₂/n-InP pseudo Schottky junctions produced under the same conditions. *Journal of Anatolian Physics and Astronomy*, 3(1), 7-18.



Content of this journal is licensed under a Creative Commons Attribution-Noncommercial 4.0 International License.

Abstract

Pseudo-Schottky junctions (PSJs) on moderately doped (MD) *n*-InP were fabricated by introducing a thin *p*-TlInS₂ counter layer before the assembly of gold rectifying contact. Successively annealing treatment was applied to create a stable inversion layer at the metal-semiconductor (MS) interface. PSJs were made with a significant barrier height (BH) enhancement, typically by the value of 0.260 eV for gold Schottky gate, after the second annealing process at 200 °C in a nitrogen atmosphere for 5 minutes. Junction parameters such as BH, ideality factor (*n*) and serial resistance (*R_s*) of identically fabricated (18 dots) Au/*p*-TlInS₂/*n*-InP PSJs have been computed by thermionic emission (TE) theory from current-voltage (*I*-*V*) and capacitance-voltage (*C*-*V*) characteristics, at room temperature and in the dark. BHs derived from *I*-*V* and *C*-*V* characteristics varied from 0.620 to 0.844 eV and 0.669 to 0.973 eV, respectively. In addition, the values of *n* varied from 1.023 to 1.706 and the serial resistances *R_s* varied from 28.3 to 131 Ω. Since all parameters of PSJs differ from one junction to another, even if they are prepared under the same conditions, a statistical study was made on the junction parameters using Tung's model. The mean values of the experimental BH, the ideality factor, and the series resistance data, which were fitted by the Gaussian function, were found to be $\bar{\phi}_{I-V} = (0.755 \pm 0.059)$ eV, $\bar{\phi}_{C-V} = (0.803 \pm 0.078)$ eV, $n = (1.384 \pm 0.152)$ and $R_s = (88.4 \pm 28.0)\Omega$, respectively. The lateral homogeneous BH ($\phi_{hom.}$) value of 0.800 eV for the Au/*p*-TlInS₂/*n*-InP junctions has been obtained from the $\phi_{eff.}$ -*n* plot by using $n_{imf.} = 1.006$ and $\Delta\phi_{imf.} = 18.0$ meV. It has been seen that the mean BH obtained from the *C*-*V* measurements correlates well with the value of $\phi_{hom.}$. The good agreement in these parameters indicates that the BH inhomogeneity observed in the Au/*p*-TlInS₂/*n*-InP PJ can be described by considering the spatial distribution hypothesis of BH put forward by Tung.

Keywords: n-InP, p-TlInS₂, pseudo-Schottky junction, I-V and C-V measurement, barrier inhomogeneities, Tung's model

Öz

Au/*p*-TlInS₂/*n*-InP Psödo-Schottky (PS) eklemleri, ön yüzüne omik kontak yapılmış *n*-InP altlığın arka yüzüne altın (Au) doğrultucu kontak imalatından önce ince *p*-TlInS₂ inversiyon tabakası büyütülerek üretildi. Metal-yarı iletken arayüzeyinin kararlılığı için ardışık tavlama işlemi uygulandı. Azot gazı atmosferinde 200 °C'de 5 dakika süreli ardışık ikinci tavlama işleminden sonra engel yüksekliğinde (EY) yaklaşık 0,260 eV'luk bir artış gözlemlendi. Aynı şartlarda üretilmiş (18 nokta) Au/*p*-TlInS₂/*n*-InP PS eklemlerinin EY, idealite faktörü (*n*) ve seri direnc (*R_s*) parametreleri Termiyonik Emisyon (TE) teorisi kullanılarak oda sıcaklığı ve karanlıkta ölçülmüş akım-voltaj (*I*-*V*) ve kapasite-voltaj (*C*-*V*) karakteristiklerinden hesaplandı. *I*-*V* ve *C*-*V* karakteristiklerinden hesaplanan EY sırasıyla (0.620-0.844) eV ve (0.669-0.973) eV, idealite faktörü *n* (1.023-1.706) ve *R_s* seri direnç değerleri ise (28.3-131) Ω aralığında değişim sergilemektedir. Aynı koşullar altında hazırlanmalarına rağmen PS eklemlerin karakteristik parametreleri kendileri arasında farklılık gösterdiğinden, eklem parametreleri üzerinde Tung modeli kullanılarak istatistiksel bir çalışma yapıldı. Gauss fonksiyonu ile fit edilen EY, *n* ve *R_s* verilerinin ortalama değerleri sırasıyla $\bar{\phi}_{I-V} = (0.755 \pm 0.059)$ eV, $\bar{\phi}_{C-V} = (0.803 \pm 0.078)$ eV, $n = (1.384 \pm 0.152)$ and $R_s = (88.4 \pm 28.0)\Omega$ olarak elde edildi. Au/*p*-TlInS₂/*n*-InP PS eklemi için yanıl homojen EY ($\phi_{hom.}$), $n_{imf.} = 1.006$ ve $\Delta\phi_{imf.} = 18.0$ meV değerleri kullanılarak $\phi_{eff.}$ -*n* çiziminden $\phi_{hom.} = 0.800$ eV olarak elde edilmiştir. *C*-*V* ölçümlerinden elde edilen ortalama EY değeri $\phi_{hom.}$ ile oldukça uyum içindedir. Parametrelerdeki bu uyum, Au/*p*-TlInS₂/*n*-InP PS ekleminde gözlenen EY inhomojenliğinin Tung tarafından ileri sürülen EY'nin uzaysal dağılımı hipotezi dikkate alınarak açıklanabileceğini gösterir.

Anahtar Kelimeler: n-InP, p-TlInS₂, pseudo Schottky eklem, I-V and C-V ölçümü, engel inhomojenliği, Tung modeli

Introduction

Indium Phosphide (InP) is one of the significant materials for high-speed and low-power device applications. Effective Schottky BH, in general, is restricted to within 0.3-0.5 eV range for n -InP independently from the contact metal and the performance of n -InP based microelectronic devices has been severely hindered (Brillson & Brucker, 1982; Hudait et al., 2001a; Hudait & Krupanidhi, 2001b; McCafferty et al., 1996). The reason for this is a high density of surface states existing at the metal/semiconductor interface. Therefore, these low barriers result a large reverse leakage current and bad electrical performance for Schottky barrier diodes (SBDs) made on n -InP. So, one of the essentialities for the InP-based devices is forming a high-quality junction with a high BH and a low ideality factor.

One of the methods for improving the effective BH is to fabricate a metal-insulator-semiconductor (MIS) structure (Sugino et al., 1990), while another one is to release the surface Fermi level pinning and use a gate metal with high work function for rectifying contact (Sugino et al., 1993). An enhancement of the BH up to 0.7-0.8 eV has been achieved by fabricating MIS Schottky junctions based on InP (Sugino et al., 1990). Assuming that the surface Fermi level pinning is pondered by high surface state density, passivation procedures by using various organic molecules have been applied to reduce the surface states of InP too (Çakar et al., 2002; Gupta & Singh, 2005; Kaya et al., 2007; Maeda et al., 1998; Schwartzman et al., 2001; Soylu et al., 2011). On the other hand, to enhance the effective BH of the n -InP based device, new energy levels in the semiconductor have been introduced to modify the band bending near the metal-semiconductor (MS) interface. This procedure is performed by creating a thin layer having opposite type doping to that of the substrate material between the substrate and the contact metal. The device, which has a hybrid structure between the p-n junction and the Schottky diode, is called pseudo-Schottky junction (PSJ) (Campbell et al., 1996; Clausen & Leistiko, 1993; Osvald & Horvath, 2004; Rhoderick & Williams, 1988; Sze, 1981). Therefore, with an increment as $\Delta\phi_{b0}$ compared to the initial BH ϕ_{b0} of typical SBDs, PSJs can have new functions not realized by a conventional Schottky device.

Thermionic emission (TE) theory is used to extract the SBD parameters (Rhoderick & Williams, 1988; Sze, 1981). Generally, non-ideal current-voltage (I - V) characteristics of a MS interface show itself with a double diode behavior (knee effect) and a slight curvature in the semi-log I - V plot. Double diode property is defined by an abnormal high current at low forward bias values and modeled as considering low barrier (LB) patches embedded within a homogeneous high barrier (HB) region. The laterally nanoscale variations of the BH, *i.e.* patchy interfaces, lead to small BHs/high ideality factors, or vice versa (Tung, 1992; Sullivan et al., 1998). Recently, a plot of effective BH versus ideality factors n that evaluated from the I - V characteristic of a set of identically fabricated diodes on a substrate has been used to explain the BH inhomogeneities (Kampen & Mönch, 1995; Leroy et al., 2005).

The layered ternary crystals with chemical formula $TlBX_2$, B=Ga or In and X=S, Se or Te, have attracted increasing interest due to their 2D structural properties and great potential applications in nanoelectronics (Abay et al., 2000a; Abay et al., 2001a; Abay et al., 2001b; Abay et al., 2001c; Abay et al., 2003; Lee, 1976; Çankaya & Abay, 2006; Güder et al 2001; Leith, 1977). 2D layers are joined to each other along the c -axis, *i.e.* perpendicular to layers, by weak interlayer Van der Waals-like interactions (Abay et al., 2000b). Crystals can easily be cleaved across this van der Waals gap resulting in mirror-like outer surfaces that closely resemble inner surfaces. The van der Waals planes are free of dangling bonds and very inert to chemical reactions, and hence the layered compounds can be considered as most suitable materials to investigate the basic features of surface or interface interactions (Lang et al., 1998). 2D $TlInS_2$ is a dichalcogenide p -type semiconductor with a direct band gap of about 2.27-2.47 eV at room temperature (Gasanly, 2010). As mentioned above, although a number of methods such as oxidation, passivation, and low-temperature deposition methods, etc., (Campbell et al., 1996; Çakar et al., 2002; Gupta & Singh, 2005; Kaya et al., 2007; Maeda et al., 1998; Osvald & Horvath, 2004; Schwartzman et al., 2001; Soylu et al., 2011; Sugino et al., 1990; Sugino et al., 1993) have been attempted for improving the characteristic parameters of devices fabricated on n -InP, to our knowledge, p - $TlInS_2/n$ -InP system has not been tested yet. In this work, we investigated experimentally whether the p - $TlInS_2$ layered ternary compound behaves as an opposite counter layer on n -InP for producing a PSJ or not. For this purpose, p - $TlInS_2/n$ -InP PSJs were fabricated by introducing a thin p - $TlInS_2$ counter layer on the moderately doped (MD) n -InP substrate before the assembly of rectifying contact. Electrical characterization of the PSJs prepared has been investigated by I - V and capacitance-voltage (C - V) measurement at room temperature and in the dark. Our main aim is to investigate statistically whether or not the effective BHs, ideality factors n , and serial resistance (R_s) obtained from the electrical characterization differ from one to the other even if the PSJs were identically prepared, by

using Tung's model.

Material and Methods

Single crystals of TlInS₂ compound were grown by the directional freezing technique, from stoichiometric high-purity elements sealed in an evacuated and carbon-coated tubular quartz ampoule with a special tip at the bottom. Details of the crystal growth procedure are reported elsewhere (Abay, 1994). The PSJs have been prepared on 12x8 mm² substrate sliced from a 2 in. moderately S-doped (1.2x10¹⁶ cm⁻³) one-side polished *n*-type InP (100) wafer. The substrate was successively cleaned with trichloroethylene/acetone/methanol and then rinsed in deionized water for 5 minutes after each step. The native oxide on the surface was then etched in sequence with acid solutions (H₂SO₄:H₂O₂:H₂O=3:1:1) and (HF (49%):H₂O=1:1) for one minute, respectively. The substrate was blow-dried with pure nitrogen gas after a rinse in deionized water and then transferred to the vacuum chamber immediately for metalizing. High-quality ohmic contact was produced by evaporating of Au:Ge eutectic alloy (88 % Au: 12 % Ge) on the unpolished (back) side of the substrate, followed by annealing at 400 °C for 3 minutes in the pure nitrogen ambient. The substrate with ohmic contact was sliced into two pieces and *p*-TlInS₂ compound was deposited onto the front surface of one of the pieces to produce a counter layer. Ex-situ annealing has been carried out at 200 °C for 5 minutes in nitrogen flow to serve as an inversion layer. After all this, Au upper contacts as 600 μm diameter circular dots were deposited on the surfaces of the untreated and the opposite doping layered i.e., contoured, substrates to form Au/*n*-InP (control device) and Au/*p*-TlInS₂/*n*-InP PSJs through a molybdenum mask at the same stage. All of the deposition processes were performed under a pressure of less than 2x10⁻⁶ mbar in the Leybold-Heraeus Univex 300 vacuum-coating unit. Substrates contain 15 or more Au/*n*-InP and Au/*p*-TlInS₂/*n*-InP devices. Successively annealing treatment was applied for improving the Au/*p*-TlInS₂/*n*-InP device characteristics. PSJs were achieved with a significant BH, typically by the value of 0.260 eV for Au Schottky gate, after second annealing process at 200 °C in nitrogen ambient for 5 minutes. *I*-*V* and *C*-*V* measurements were performed by a computer-controlled Keithley 487 picoammeter-voltage source and an HP 4192A LF impedance analyzer at room temperature and in the dark.

Results and Discussion

The characteristic parameters of the devices were investigated using the *I*-*V* and *C*-*V* characteristics. The current (*I*) through a device a forward bias (*V*), according to thermionic emission (TE) theory, is given by (Rhoderick & Williams, 1998; Sze, 1981)

$$I = I_0 \exp\left(\frac{qV}{nkT}\right) \left[1 - \exp\left(-\frac{qV}{kT}\right) \right] \quad (1)$$

where *q*, *V*, *n*, *k*, and *T*, are the electronic charge, the applied bias voltage, the ideality factor, the Boltzmann constant, and the absolute temperature in Kelvin, respectively, and *I*₀ is the saturation current derived from the straight-line intercept of ln(*I*)-*V* plot at zero-bias defined by:

$$I_0 = AA^*T^2 \exp\left(-\frac{q\phi_{b0}}{kT}\right). \quad (2)$$

where *A* (= 2.83x10⁻⁷ m²) is the effective diode area, *A*^{*} (= 9.40 AK⁻²cm⁻² for *n*-type InP) is the effective Richardson constant, *φ*_{b0} is the zero-bias current-BH (apparent or measured BH) which can be obtained using the following equation by using the determined value of *I*₀:

$$\phi_{b0} = kT \ln\left(\frac{AA^*T^2}{I_0}\right). \quad (3)$$

The ideality factor (*n*) of a Schottky barrier diode is described the deviation of experimental *I*-*V* data from the TE theory. Considering the deviation of the experimental *I*-*V* data from the ideal TE theory a slop parameter (ideality factor *n*)

is introduced to Eq. (1). Using the definition, ideality factor can be expressed as:

$$n = \frac{q}{kT} \left(\frac{dV}{d \ln(I)} \right) \quad (4)$$

On the other hand, by neglecting the image-force barrier lowering ($\Delta\phi_{if}$), capacitance-voltage BH (ϕ_{CV}) for a MS device fabricated on an n -type semiconductor can be expressed as (Rhoderick & Williams, 1998; Sze, 1981):

$$\phi_{C-V} = V_{bi} + \frac{kT}{q} \left[1 + \ln \frac{N_c}{N_i} \right] \quad (5)$$

where, V_{bi} is the built-in voltage determined from the extrapolation of the C^2 - V plot to the voltage axis, N_c ($=5.47 \times 10^{17} \text{ cm}^{-3}$) is the effective density of states in the conduction band for n -InP at 300 K (Donald, 1982; Singh, 2001) and N_i is the concentration of the non-compensated ionized donors, respectively.

Fig. 1 shows typically experimental semilog forward and reverse bias I - V characteristics for Au/ n -InP SBD and Au/ p -TlInS₂/ n -InP PSJ at room temperature and in the dark. As can be seen from Fig. 1, the forward I - V characteristic of the Au/ p -TlInS₂/ n -InP PSJ also shows the rectifying behavior and the reverse curve exhibits slightly soft behavior in which the current does not saturate to a constant value. The apparent BHs of the devices were calculated from the y -axis intercepts of the semilog forward bias I - V characteristics according to Eq. (3). The values of n were calculated from the slope of the linear regions of the forward I - V characteristics according to Eq. (4).

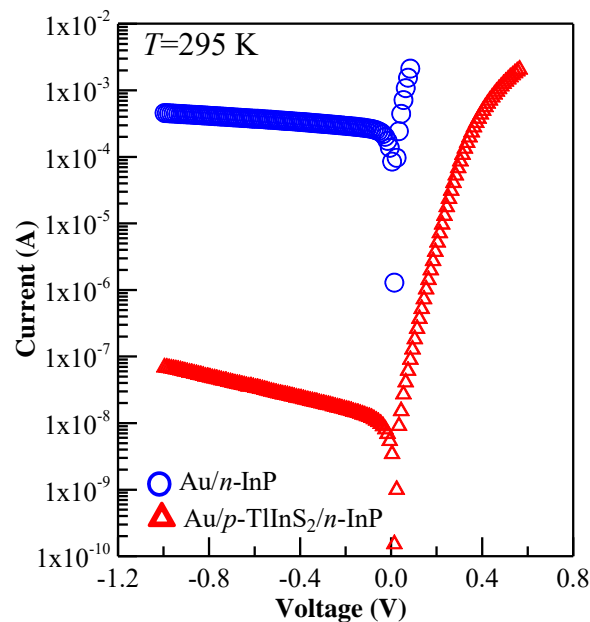


Figure 1. I - V characteristics for typical Au/ n -InP SBD and Au/ p -TlInS₂/ n -InP PSJ at room temperature

The extrapolation of the I - V curves to zero-bias yields the value of saturation current as 1.09×10^{-4} and 4.26×10^{-9} A for the reference Au/ n -InP SBD and Au/ p -TlInS₂/ n -InP PSJ, respectively. As can be seen from these data, the presence of an intentionally grown opposite-type counter layer on the n -InP reduces the value of saturation current by about four orders of magnitude, indicating an increase in the BH. The values of current BH for the reference and Au/ p -TlInS₂/ n -InP PSJ were calculated as 0.429 and 0.687 eV, respectively. The values of ϕ_{b0} are the effective values and do not consider the image-force lowering. The apparent BH of 0.429 eV for the reference diode is in close agreement with the previously published data (Brillson & Brucker, 1982; Campbell et al., 1996; Shi et al., 1991; Chou et al., 1998; Çakar et al., 2002; Gupta & Singh, 2005; Hökelek & Robinson, 1981; Hudait et al., 2001a; Hudait & Krupanidhi, 2001b; İsmail et al., 1987; Kaya et al., 2007; Maeda et al., 1998; McCafferty et al., 1996; Schwartzman et al., 2001; Soylu et al., 2011; Soylu & Abay, 2009; Sugino et al., 1990; Sugino et al., 1993).

From the slope of the I - V curves, the ideality factors were obtained as 1.002 and 1.066 for the reference and Au/ p -TlInS₂/ n -InP PSJ, respectively. The low ideality factors ($n \leq 1.10$) indicate that TE is the dominant transport mechanism for all devices. As can be seen, the leakage current has been reduced after the surface modification of n -InP by TlInS₂ deposition, effectively giving an increased BH, accompanied by a little departure of the ideality factor (1.066) from unity. The increase in the BH was about 260 meV.

The effective BH and n values were obtained as many as 18 Au/ p -TlInS₂/ n -InP PSJ, from individual I - V characteristics via Eq. (3) and (4), respectively (Fig. 2). The BHs for the diodes varied from 0.620 to 0.844 eV while, the values of ideality factor n varied from 1.023 to 1.706. It is seen clearly that our PSJs have significantly larger ideality factors.

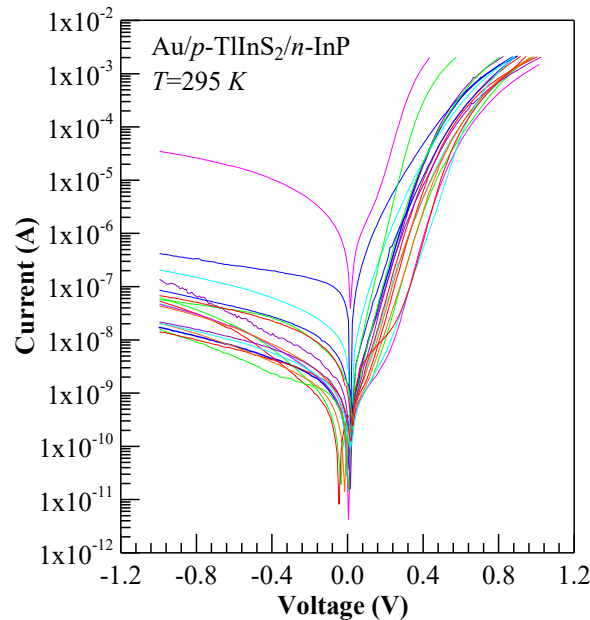


Figure 2. Experimental forward and reverse bias I - V characteristic for eighteen Au/ p -TlInS₂/ n -InP PSJs at room temperature

The results showed that both parameters of SBDs differ from one device to another even if they are identically prepared. Therefore, the first and common practice comes to mind to average these values. However, it is highly important to understand both the physical origin of such differences in the conventional parameters of SBDs and of non-ideal behavior in I - V characteristics for improving future device applications. Tung's inhomogeneity model proposes that this non-ideal behavior could be explained quantitatively by considering the specific distribution of nanometer-scale interfacial patches of reduced BH (Tung, 1992). The inhomogeneity model is based on small local regions or patches on the lateral contact area. Non-uniformity of the interfacial charges, interfacial oxide layer thickness, grain boundaries, multiple phases, facets, defects mixing phases, etc. causes this inhomogeneity offered by a vast of researchers (Im et al., 2001; Kampen & Mönch, 1995; Leroy et al., 2005; Mönch, 1999; Mönch, 2001; Schmitsdorf et al., 1998; Sze, 1981; Sullivan et al., 1998; Tung, 1992).

The ideality factor (n) of a MS device represents a direct measure of the interface uniformity. In general, the values of n greater than unity sign to the presence of a lateral inhomogeneous distribution of BHs at the MS interface. To date, the existence of a linear correlation between the effective BH and the ideality factor n in different diode sets prepared on various semiconductor substrates has been reported in many studies (Im et al., 2001; Mönch, 1999; Mönch, 2001; Schmitsdorf et al., 1998).

In Fig. 3, effective BHs versus ideality factory values (ϕ_{eff} vs n plot) are given. As can be seen from this figure, the BHs become smaller mutually as the ideality factors increase and there is a linear relationship between the experimental effective BHs and the experimental ideality factors for the Au/ p -TlInS₂/ n -InP PSJs that have been explained by lateral inhomogeneities of the BHs (Im et al., 2001; Kampen & Mönch, 1995; Leroy et al., 2005; Mönch, 1999; Mönch, 2001; Schmitsdorf et al., 1998; Sullivan et al., 1998; Sze, 1981; Tung, 1992).

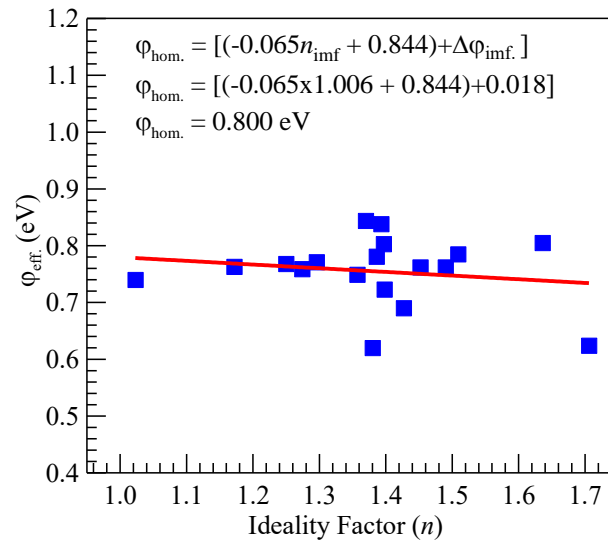


Figure 3. Effective BHs versus ideality factors (ϕ_{eff} vs n) of the identically prepared eighteen Au/p-TlInS₂/n-InP PSJs

It has been mentioned in the related studies that (Im et al., 2001; Kampen & Mönch, 1995; Leroy et al., 2005; Mönch, 1999; Mönch, 2001; Schmitsdorf et al., 1998; Sullivan et al., 1998; Sze, 1981; Tung, 1992) the higher values of n among identically prepared diodes were often found to accompany lower BHs. The straight line in Fig. 3 is least square fitting curve to the experimental data. Therefore, it can be concluded that our Au/p-TlInS₂/n-InP PSJ are patchy (Im et al., 2001; Mönch, 1999; Mönch, 2001; Schmitsdorf et al., 1998). The lateral homogeneous BH ($\phi_{\text{hom.}}$) value of 0.800 eV for the Au/p-TlInS₂/n-InP junctions has been obtained from the $\phi_{\text{eff.}}$ - n plot by using $n_{\text{inf.}} = 1.006$ and $\Delta\phi_{\text{inf.}} = 18.0 \text{ meV}$.

The capacitance-voltage (C-V) characteristics of the Au/p-TlInS₂/n-InP PSJ under 1.00 MHz operation frequency were also performed to get detailed information about the junction parameters. Capacitance BH ϕ_{CV} for a Schottky-type junction with the interfacial layer can be defined as the following relation (Donald, 1982; Rhoderick & Williams, 1988; Singh, 2001; Sze, 1981; Van der Ziel, 1968):

$$\phi_{\text{CV}} = \gamma V_{\text{bi}} + V_{\text{n}} + kT/q. \quad (6)$$

where, γ is the reciprocal of the ideality factor n which gives rise to voltage drop across an interfacial layer (Abay, 2015; Chand & Bala, 2007; Chattopadhyay & Daw, 1986). If γ is equal to unity, in that case, the device shows an ideal behavior. V_{n} is the energy difference between the Fermi level and the bottom of the conduction band. The ϕ_{CV} values have been obtained using the intercept voltage values (V_{bi}) determined from the reverse bias C^2 -V curves (not shown in here) and the values of γ ($=1/n$) for each Au/p-TlInS₂/n-InP PSJ via Eq. (6). Details for calculating procedure for the ϕ_{CV} values have been given by Abay (2015).

Figs. 4 and 5 show the statistical distribution of BHs evaluated from forward bias I -V and reverse bias C -V characteristics of the Au/p-TlInS₂/n-InP PSJs (18 dots), respectively. The experimental values of the effective BHs were fitted by a Gaussian function. Mean BH values were obtained as $\bar{\phi}_{\text{I-V}} = (0.755 \pm 0.059) \text{ eV}$ and $\bar{\phi}_{\text{C-V}} = (0.803 \pm 0.078) \text{ eV}$, respectively from the statistical analysis.

In Figs. 6 and 7, the statistical distribution of ideality factors and serial resistance values evaluated from the forward bias I -V characteristics of the Au/p-TlInS₂/n-InP PSJ were given, respectively. The experimental values of the n and R_{s} were fitted by a Gaussian function too. From the statistical analysis of this fit the values of the mean ideality factor and serial resistance were obtained as $n = (1.384 \pm 0.152)$ and $R_{\text{s}} = (88.4 \pm 28.0) \Omega$, respectively.

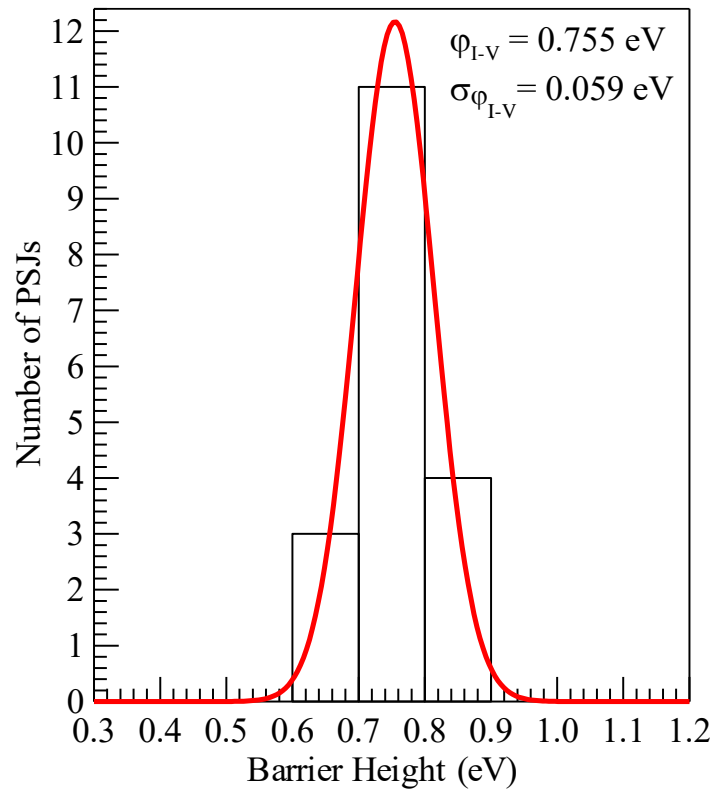


Figure 4. Gaussian distribution of effective BHs for the Au/p-TlInS₂/n-InP PSJs evaluated from forward bias *I-V* characteristics

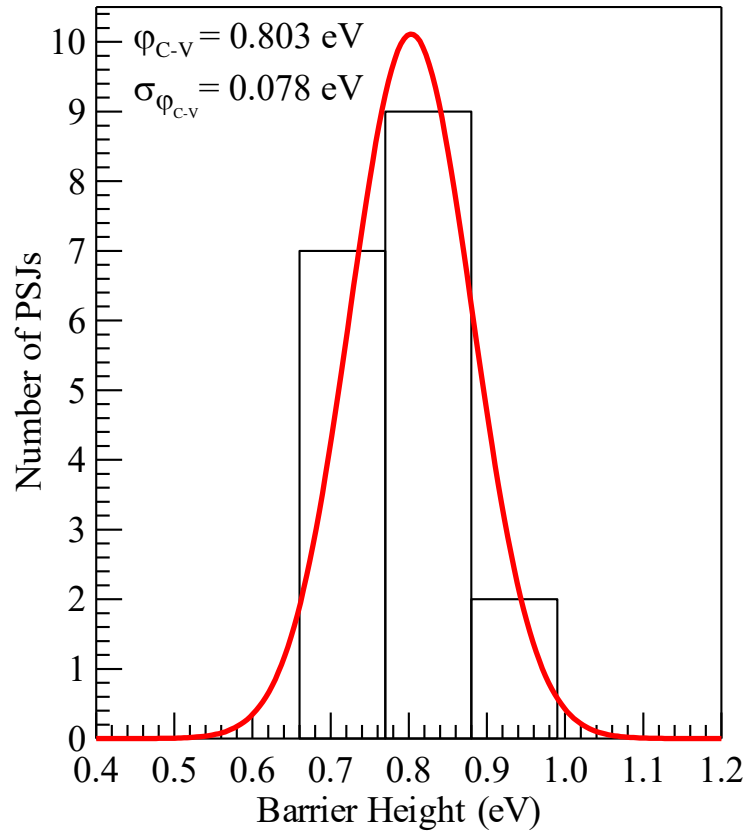


Figure 5. Gaussian distribution of BH for the Au/p-TlInS₂/n-InP PSJs evaluated from reverse bias *C-V* characteristics.

It has been seen that the mean BH obtained from the *C-V* measurements is correlated well with the value of ϕ_{hom} . The good agreement of these parameters indicates that the BH inhomogeneity of the Au/p-TlInS₂/n-InP pseudo junction

can be well described by spatial distributions of BH, that is, electron transport at the MS interface is significantly affected by nanoscale spatial variations.

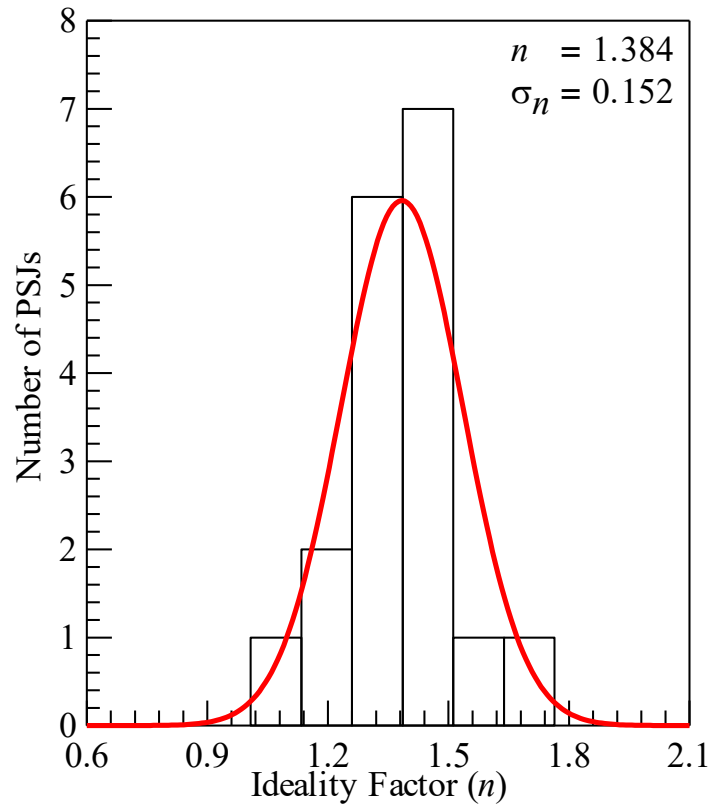


Figure 6. Gaussian distribution of the ideality factors for the Au/p-TlInS₂/n-InP PSJs evaluated from forward bias I - V characteristics

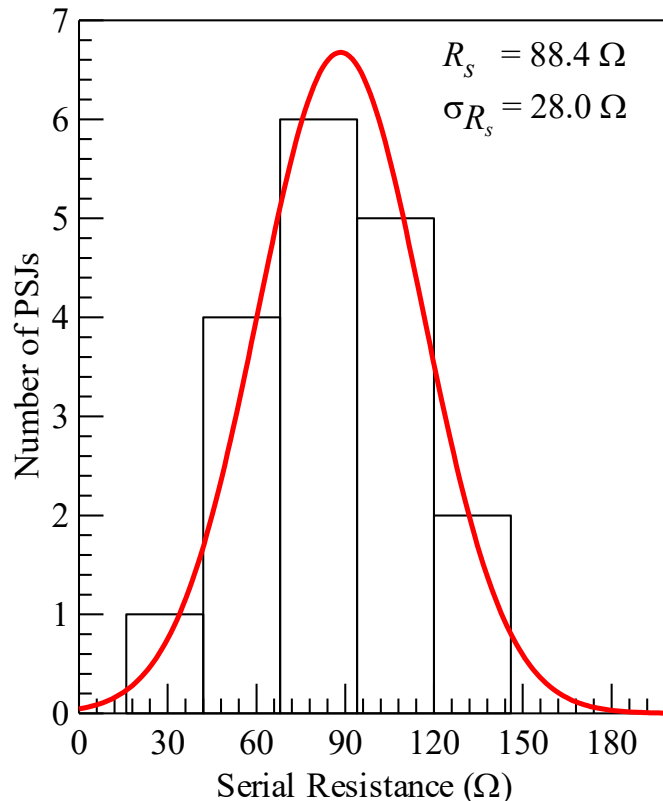


Figure 7. Gaussian distribution of the serial resistance for the Au/p-TlInS₂/n-InP PSJs evaluated from Cheung's functions

Conclusion

- Au/p-TlInS₂/n-InP PSJs have been fabricated by introducing a thin chalcogenide ternary compound counter layer of p-TlInS₂ on the MD n-InP substrate, for the first time.
- Room temperature electrical characterizations of the Au/p-TlInS₂/n-InP PSJs have been investigated by I-V and C-V measurements at and in the dark.
- Fabricated Au/p-TlInS₂/n-InP PSJs have good rectifying properties. The leakage current value of Au/p-TlInS₂/n-InP PSJ was reduced by four orders compared to the unmodified Au/n-InP structure, effectively giving an increased BH, accompanied by a little departure of the ideality factor ($n=1.066$) from unity. The increase in the BH was about 260 meV.
- Statistical investigations, by using Tung's model, showed that all parameters of PSJs differ from one junction to another even if they are identically prepared. The experimental values of BH, ideality factor, and serial resistance are fitted by a Gaussian function, and their mean values were found to be $\bar{\varphi}_{1-V} = (0.755 \pm 0.059)$ eV, $\bar{\varphi}_{C-V} = (0.803 \pm 0.078)$ eV, $n = (1.384 \pm 0.152)$ and $R_s = (88.4 \pm 28.0) \Omega$, respectively. A lateral homogeneous BH ($\varphi_{\text{hom.}}$) value of 0.800 eV for the Au/p-TlInS₂/n-InP junctions has been obtained from the $\varphi_{\text{eff.}}$ vs. n plot by using $n_{\text{inf.}} = 1.006$ and $\Delta\varphi_{\text{inf.}} = 18.0$ meV.

From the good agreement with the values of $\varphi_{\text{hom.}}$ and $\bar{\varphi}_{C-V}$ it has been concluded that BH inhomogeneity of Au/p-TlInS₂/n-InP junction can be well described by spatial distributions of BH considering based on the TE mechanisms.

Hakem Değerlendirmesi: Dış bağımsız.

Yazar Katkıları: Fikir-BA; Tasarım-BA; Denetleme-BA; Kaynaklar-SY,FA,ANB,NK,DA; Veri Toplanması ve/veya İşlemesi-SY,FA,ANB,NK,DA; Analiz ve/veya Yorum-BA,SY,FA,,ANB,NK,DA; Literatür Taraması-BA,SY,FA,ANB,NK,DA; Yazıyı Yazan-BA,SY; Eleştirel İnceleme-BA,SY,FA,ANB,NK,DA; Diğer-BA

Çıkar Çatışması: Yazarlar, çıkar çatışması olmadığını beyan etmiştir.

Finansal Destek: Yazarlar, bu çalışma için finansal destek almadığını beyan etmiştir.

Peer-review: Externally peer-reviewed.

Author Contributions: Concept -BA; Design-BA; Supervision-BA; Resources--SY,FA,ANB,NK,DA; Data Collection and/or Processing- SY,FA,ANB,NK,DA; Analysis and/or Interpretation- BA,SY,FA,ANB,NK,DA; Literature Search-BA,SY,FA,ANB,NK,DA; Writing Manuscript-BA,SY; Critical Review- BA,SY,FA,ANB,NK,DA; Other-BA

Conflict of Interest: The authors have no conflicts of interest to declare.

Financial Disclosure: The authors declared that this study has received no financial support.

References

- Abay, B. (2015). Barrier characteristics of biopolymer-based organic/inorganic Au/CTS/n-InP hybrid junctions. *The Philosophical Magazine a Journal of Theoretical Experimental and Applied Physics*, 95(31), 3413–3428. <https://doi.org/10.1080/14786435.2015.1076583>
- Abay, B., Ankaya, G., Der, H. S. G., Efeoglu, H., & U, Y. K. Y. (2002). Barrier characteristics of Cd/p-GaTe Schottky diodes based on I-V measurements. *Semiconductor Science and Technology*, 18(2), 75–81. <https://doi.org/10.1088/0268-1242/18/2/302>
- Abay, B., Efeoglu, H., Yogurtçu, Y. K., & Alieva, M. (2001b). Low-temperature visible photoluminescence spectra of Tl₂GaInSe₄ layered crystals. *Semiconductor Science and Technology*, 16(9), 745–749. <https://doi.org/10.1088/0268-1242/16/9/302>
- Abay, B., Güder, H., Efeoglu, H., & Yoğurtçu, Y. (2001a). Temperature dependence of the optical energy gap and Urbach–Martienssen's tail in the absorption spectra of the layered semiconductor Tl₂GaInSe₄. *Journal of Physics and Chemistry of Solids*, 62(4), 747–752. [https://doi.org/10.1016/s0022-3697\(00\)00236-5](https://doi.org/10.1016/s0022-3697(00)00236-5)
- Abay, B., Güder, H. S., Efeoglu, H., & Yogurtçu, Y. K. (2000b). Excitonic absorption and Urbach-Martienssen tails in Gd-doped and undoped p-type GaSe. *Semiconductor Science and Technology*, 15(6), 535–541. <https://doi.org/10.1088/0268-1242/15/6/308>

Abay, B., Güder, H., Efeoğlu, H., & Yoğurtçu, Y. (2001c). Urbach-Martienssen Tails in the Absorption Spectra of Layered Ternary Semiconductor TlGaS₂. *Physica Status Solidi. B, Basic Research*, 227(2), 469–476. [https://doi.org/10.1002/1521-3951\(200110\)227:2](https://doi.org/10.1002/1521-3951(200110)227:2)

Abay, B., Onganer, Y., Sağlam, M., Efeoğlu, H., Türüt, A., & Yoğurtçu, Y. (2000a). Current–voltage and capacitance–voltage characteristics of metallic polymer/InSe(:Er) Schottky contacts. *Microelectronic Engineering*, 51–52, 689–693. [https://doi.org/10.1016/s0167-9317\(99\)00532-8](https://doi.org/10.1016/s0167-9317(99)00532-8)

Abay, A. (1994). Growth and investigation for some optical and electrical properties of TlInSe₂ and TlGaSe₂ ternary layered semiconductor crystals as a function of temperature, PhD Thesis (in Turkish), Atatürk University Graduate School of Natural & Applied Science Erzurum, Turkey (unpublished).

Brillson, L. J., Brucker, C. F., Katnani, A. D., Stoffel, N. G., Daniels, R., & Margaritondo, G. (1982). Fermi-level pinning and chemical structure of InP–metal interfaces. *Journal of Vacuum Science & Technology/Journal of Vacuum Science and Technology*, 21(2), 564–569. <https://doi.org/10.1116/1.571764>

Campbell, I. H., Rubin, S., Zawodzinski, T. A., Kress, J. D., Martin, R. L., Smith, D. L., Barashkov, N. N., & Ferraris, J. P. (1996). Controlling Schottky energy barriers in organic electronic devices using self-assembled monolayers. *Physical Review. B, Condensed Matter*, 54(20), R14321–R14324. <https://doi.org/10.1103/physrevb.54.r14321>

Chand, S., & Bala, S. (2007). Simulation studies of current transport in metal–insulator–semiconductor Schottky barrier diodes. *Physica. B, Condensed Matter*, 390(1–2), 179–184. <https://doi.org/10.1016/j.physb.2006.08.011>

Chattopadhyay, P., & Daw, A. (1986). On the current transport mechanism in a metal–insulator–semiconductor (MIS) diode. *Solid-state Electronics*, 29(5), 555–560. [https://doi.org/10.1016/0038-1101\(86\)90078-x](https://doi.org/10.1016/0038-1101(86)90078-x)

Chou, L. J., Hsieh, K. C., Wohlert, D. E., Cheng, K. Y., & Finnegan, N. (1998). Formation of amorphous aluminum oxide and gallium oxide on InP substrates by water vapor oxidation. *Journal of Applied Physics*, 84(12), 6932–6934. <https://doi.org/10.1063/1.368993>

Clausen, T., & Leistiko, O. (1993). High effective Schottky barriers on n-type InP using Zn-based metallizations and rapid thermal annealing. *Semiconductor Science and Technology*, 8(9), 1731–1740. <https://doi.org/10.1088/0268-1242/8/9/011>

Çakar, M., Türüt, A., & Onganer, Y. (2002). The Conductance- and Capacitance-Frequency Characteristics of the Rectifying Junctions Formed by Sublimation of Organic Pyronine-B on p-Type Silicon. *Journal of Solid State Chemistry*, 168(1), 169–174. <https://doi.org/10.1006/jssc.2002.9706>

Çankaya, G., & Abay, B. (2005). Current- and capacitance-voltage characteristics of Cd/p-GaTe Schottky barrier diodes under hydrostatic pressure. *Semiconductor Science and Technology*, 21(2), 124–130. <https://doi.org/10.1088/0268-1242/21/2/004>

Donald, A.N. (1982). *Semiconductor Physics and Devices*, (Boston, Irwin).

Gasanly, N. M. (2010). Coexistence of Indirect and Direct Optical Transitions, Refractive, Index and Oscillator Parameters in TlGaS₂, TlGaSe₂, and TlInS₂ Layered Single Crystals. *Journal of the Korean Physical Society*, 57(1), 164–168. <https://doi.org/10.3938/jkps.57.164>

Güder, H., Abay, B., Efeoğlu, H., & Yoğurtçu, Y. (2001). Photoluminescence characterization of GaTe single crystals. *Journal of Luminescence*, 93(3), 243–248. [https://doi.org/10.1016/s0022-2313\(01\)00192-2](https://doi.org/10.1016/s0022-2313(01)00192-2)

Gupta, R. K., & Singh, R. A. (2005). Junction properties of Schottky diode based on composite organic semiconductors: Polyaniline-polystyrene system. *Journal of Polymer Research*, 11(4), 269–273. <https://doi.org/10.1007/s10965-005-2412-2>

Hökelek, E., & Robinson, G. (1981). A comparison of Pd Schottky contacts on InP, GaAs and Si. *Solid-state Electronics*, 24(2), 99–103. [https://doi.org/10.1016/0038-1101\(81\)90001-0](https://doi.org/10.1016/0038-1101(81)90001-0)

Hudait, M., & Krupanidhi, S. (2001b). Doping dependence of the barrier height and ideality factor of Au/n-GaAs Schottky diodes at low temperatures. *Physica. B, Condensed Matter*, 307(1-4), 125–137. [https://doi.org/10.1016/s0921-4526\(01\)00631-7](https://doi.org/10.1016/s0921-4526(01)00631-7)

Hudait, M., Venkateswarlu, P., & Krupanidhi, S. (2001a). Electrical transport characteristics of Au/n-GaAs Schottky diodes on n-Ge at low temperatures. *Solid-state Electronics*, 45(1), 133–141. [https://doi.org/10.1016/s0038-1101\(00\)00230-6](https://doi.org/10.1016/s0038-1101(00)00230-6)

Im, H. J., Ding, Y., Pelz, J. P., & Choyke, W. J. (2001). Nanometer-scale test of the Tung model of Schottky-barrier height inhomogeneity. *Physical Review. B, Condensed Matter*, 64(7). <https://doi.org/10.1103/physrevb.64.075310>

Ismail, A., Brahim, A. B., Dumas, M., & Lassabatere, L. (1987). The interaction of Ag and Al overlayers with InP (110): Surface and diode studies of the effect of Sb interlayers. *Journal of Vacuum Science & Technology. B, Microelectronics*

Processing and Phenomena, 5(3), 621–623. <https://doi.org/10.1116/1.583793>

Kampen, T., & Mönch, W. (1995). Lead contacts on Si(111):H-1 × 1 surfaces. *Surface Science*, 331–333, 490–495. [https://doi.org/10.1016/0039-6028\(95\)00079-8](https://doi.org/10.1016/0039-6028(95)00079-8)

Kaya, M., Çetin, H., Boyarbay, B., Gök, A., & Ayyildiz, E. (2007). Temperature dependence of the current–voltage characteristics of Sn/PANI/p-Si/Al heterojunctions. *Journal of Physics. Condensed Matter*, 19(40), 406205. <https://doi.org/10.1088/0953-8984/19/40/406205>

Lang, O., Schlaf, R., Tomm, Y., Pettenkofer, C., & Jaegermann, W. (1994). Single crystalline GaSe/WSe₂ heterointerfaces grown by van der Waals epitaxy. I. Growth conditions. *Journal of Applied Physics*, 75(12), 7805–7813. <https://doi.org/10.1063/1.356562>

Lee, P. A. (1976). *Optical and Electrical Properties*.

Leroy, W., Opsomer, K., Forment, S., & Van Meirhaeghe, R. (2005). The barrier height inhomogeneity in identically prepared Au/n-GaAs Schottky barrier diodes. *Solid-state Electronics*, 49(6), 878–883. <https://doi.org/10.1016/j.sse.2005.03.005>

Lieth, R. M. A. (2014). *Preparation and Crystal Growth of Materials with Layered Structures*.

Maeda, F., Watanabe, Y., & Oshima, M. (1993). Surface chemical bonding of (NH₄)₂Sx-treated InP(001). *Applied Physics Letters*, 62(3), 297–299. <https://doi.org/10.1063/1.108996>

McCafferty, P., Sellai, A., Dawson, P., & Elabd, H. (1996). Barrier characteristics of Schottky diodes as determined from I-V-T measurements. *Solid-state Electronics*, 39(4), 583–592. [https://doi.org/10.1016/0038-1101\(95\)00162-x](https://doi.org/10.1016/0038-1101(95)00162-x)

Mönch, W. (1999). Barrier heights of real Schottky contacts explained by metal-induced gap states and lateral inhomogeneities. *Journal of Vacuum Science & Technology. B, Microelectronics and Nanometer Structures*, 17(4), 1867–1876. <https://doi.org/10.1116/1.590839>

Mönch, W. (2001). Semiconductor Surfaces and Interfaces. In *Springer series in surface sciences*. <https://doi.org/10.1007/978-3-662-04459-9>

Osvald, J., & Horváth, Z. (2004). Theoretical study of the temperature dependence of electrical characteristics of Schottky diodes with an inverse near-surface layer. *Applied Surface Science*, 234(1–4), 349–354. <https://doi.org/10.1016/j.apsusc.2004.05.046>

Rhoderick, E. H., & Williams, R. H. (1988). *Metal-semiconductor Contacts*. Oxford University Press, USA.

Schmitsdorf, R. F., Kampen, T. U., & Mönch, W. (1997). Explanation of the linear correlation between barrier heights and ideality factors of real metal-semiconductor contacts by laterally nonuniform Schottky barriers. *Journal of Vacuum Science & Technology. B, Microelectronics and Nanometer Structures*, 15(4), 1221–1226. <https://doi.org/10.1116/1.589442>

Schvartzman, M., Sidorov, V., Ritter, D., & Paz, Y. (2001). Surface passivation of (100) InP by organic thiols and polyimide as characterized by steady-state photoluminescence. *Semiconductor Science and Technology*, 16(10), L68–L71. <https://doi.org/10.1088/0268-1242/16/10/103>

Shi, Z. Q., Wallace, R. L., & Anderson, W. A. (1991). High-barrier height Schottky diodes on N-InP by deposition on cooled substrates. *Applied Physics Letters*, 59(4), 446–448. <https://doi.org/10.1063/1.105458>

Singh, J. (2000). *Semiconductor Devices*. John Wiley & Sons.

Soylu, M., & Abay, B. (2009). Barrier characteristics of gold Schottky contacts on moderately doped n-InP based on temperature dependent I–V and C–V measurements. *Microelectronic Engineering*, 86(1), 88–95. <https://doi.org/10.1016/j.mee.2008.09.045>

Soylu, M., Abay, B., & Onganer, Y. (2011). Electrical characteristics of Au/Pyronine-B/moderately doped n-type InP Schottky structures in a wide temperature range. *Journal of Alloys and Compounds*, 509(16), 5105–5111. <https://doi.org/10.1016/j.jallcom.2011.01.183>

Sugino, T., Ito, H., & Shirafuji, J. (1990). Barrier height enhancement of InP Schottky junctions by treatment with photo-decomposed PH₃. *Electronics Letters*, 26(21), 1750. <https://doi.org/10.1049/el:19901124>

Sugino, T., Sakamoto, Y., Sumiguchi, T., Nomoto, K. N. K., & Shirafuji, J. S. J. (1993). Barrier Heights of Schottky Junctions on n-InP Treated with Phosphine Plasma. *Japanese Journal of Applied Physics*, 32(9A), L1196. <https://doi.org/10.1143/jjap.32.l1196>

Sullivan, J. P., Tung, R. T., Pinto, M. R., & Graham, W. R. (1991). Electron transport of inhomogeneous Schottky barriers: A numerical study. *Journal of Applied Physics*, 70(12), 7403–7424. <https://doi.org/10.1063/1.349737>

Sze, S. M. (1981). *Physics of Semiconductor Devices*. Wiley-Interscience.

Tung, R. T. (1992). Electron transport at metal-semiconductor interfaces: General theory. *Physical Review. B, Condensed*

Matter, 45(23), 13509–13523. <https://doi.org/10.1103/physrevb.45.13509>
Van Der Ziel, A. (1968). *Solid State Physical Electronics*. Prentice Hall.

Analyzing the Relationship Between Cosmic Rays and Total Cloud Cover with LSTM Networks

Kozmik Işınlar ve Toplam Bulut Örtüsü Arasındaki İlişkinin LSTM Ağlarıyla Analizi

Ahmet POLATOĞLU 

Atatürk University, Department of Astronomy
and Space Science, Faculty of Sciences,
Erzurum, Turkey



Abstract

Understanding the interactions between cosmic phenomena and terrestrial weather patterns, particularly the relationship between cosmic rays (CRs) and cloud cover, has been a significant scientific endeavor. CRs, high-energy particles originating from supernovae, can ionize air molecules upon entering Earth's atmosphere, potentially influencing cloud formation. Cloud cover plays a vital role in Earth's climate system by regulating energy balance through reflecting solar radiation and trapping infrared radiation. This study aims to analyze the relationship between CRs and Total Cloud Cover (TCC) globally using Long Short-Term Memory (LSTM) networks, a type of recurrent neural network suited for time series data. We used data from the University of Oulu's Cosmic Ray Station and the Copernicus Climate Change Service's ECMWF European Reanalysis V5 (ERA5). A correlation matrix was constructed to identify relationships between CRs and TCC across various regions, including the Antarctic, Arctic, Europe, and globally. The results indicated generally weak and negative correlations between CR and TCC, with weak positive correlations in the Southern Hemisphere and globally. Negative correlations were more pronounced in the Antarctic and Arctic regions, suggesting region-specific climate mechanisms. The LSTM model's predictions of CR values did not closely follow actual values, indicating a significant gap in capturing dynamic changes and peaks, and suggesting the need for more data, additional features, or further tuning. The training process showed rapid initial learning but overfitting after several epochs. The final model's performance, measured by test mean squared error (MSE), suggested inadequate generalization. These findings highlight the complexity of modeling the CR-TCC relationship using machine learning. Future research should focus on enhancing data quality, incorporating detailed cloud metrics, and exploring advanced models to better understand CRs influence on cloud formation and climate. This study contributes to the debate on CR role in climate systems, providing insights for improved climate models and predictions.

Keywords: Cosmic Ray (CR), Total Cloud Cover (TCC), Long Short-Term Memory (LSTM) Networks, Climate Modeling.

Öz

Dünya dışı radyasyon ile yeryüzündeki hava olayları arasındaki etkileşimleri, özellikle kozmik ışınlar (CR) ile bulut örtüsü arasındaki ilişkiyi anlamak, son yıllarda önemli bir bilimsel alan oluşturmuştur. Süpernova gibi kaynaklardan oluşan yüksek enerjili kozmik parçacıklar, Dünya atmosferine girdiklerinde hava moleküllerini iyonize edebilmekte ve bu da potansiyel olarak bulut oluşumunu etkileyebilmektedir. Bulut örtüsü, güneş radyasyonunu yansıtarak ve kızılötesi radyasyonu tutarak enerji dengesini düzenlediği için Dünya'nın iklimi üzerinde hayati bir rol oynar. Bu çalışma, CR ile Toplam Bulut Örtüsü (TCC) arasındaki ilişkiyi küresel ölçekte analiz etmeyi amaçlamaktadır. Bu amaçla, zaman serisi verileri için uygun bir tekrarlayan sinir ağı türü olan Uzun Kısa Dönemli Bellek (LSTM) ağları kullanılmıştır. CR verileri, Oulu Üniversitesi Kozmik Işın İstasyonu'ndan ve bulut verileri de Copernicus Climate Change Service's ECMWF European Reanalysis V5 (ERA5)'in Maine Üniversitesi climate reanalyzer sayfası üzerinden alınmıştır. CR'ler ve TCC arasındaki ilişkileri belirlemek için Antarktika, Arktik, Avrupa ve küresel dahil olmak üzere çeşitli bölgelerde bir korelasyon matrisi oluşturulmuştur. Sonuçlar, CR ve TCC arasında genellikle zayıf negatif korelasyonlar olduğunu, Güney Yarımküre ve küresel ölçekte zayıf pozitif korelasyonlar olduğunu göstermiştir. Antarktika ve Arktik bölgelerinde negatif korelasyonlar daha belirgindir ve bu da bölgeye özgü iklim mekanizmalarını işaret eder. LSTM modelinin CR değerlerinin tahminleri, dinamik değişiklikleri ve zirveleri yakalamada önemli bir boşluk olduğunu ve daha fazla veri, ek özellikler veya daha fazla parametre gereksinimi olduğunu göstererek, gerçek değerleri yakından takip etmemiştir. Eğitim süreci hızlı başlangıç öğrenmesi göstermiş ancak birkaç dönemden sonra aşırı öğrenme (overfitting) ortaya çıkmıştır. Nihai modelin performansı, test ortalama kare hatası (MSE) ile ölçüldüğünde, yetersiz genelleme yapıldığını göstermiştir. Bu bulgular, makine öğrenimi kullanarak CR-TCC ilişkisini modellemenin karmaşıklığını vurgulamaktadır. Gelecek araştırmalar, veri kalitesini artırmaya, ayrıntılı bulut metriklerini eklemeye ve CR'lerin bulut oluşumu ve iklim üzerindeki etkisini daha iyi anlamak için ileri modelleri keşfetmeye odaklanmalıdır. Bu çalışma, CR'nin iklim sistemlerindeki rolü hakkındaki tartışmalara katkıda bulunarak, daha iyi iklim modelleri ve tahminleri için öngörüler sunmaktadır.

Anahtar Kelimeler: Kozmik Işın (CR), Toplam Bulut Örtüsü (TCC), Uzun Kısa-Dönemli Bellek (LSTM) Ağları, İklim Modelleme.

Corresponding Author/ Sorumlu Yazar:

A. POLATOĞLU

E-mail:

ahmet.polatoglu@atauni.edu.tr

Received/ Geliş Tarihi 26.04.2024

Accepted/Kabul Tarihi 31.05.2024

Publication Date/ 27.06.2024

Yayın Tarihi

Cite this article

Polatoglu, A. (2024). *Analyzing the Relationship Between Cosmic Rays and Total Cloud Cover with LSTM Networks*. *Journal of Anatolian Physics and Astronomy*, 3(1), 19-26.



Content of this journal is licensed under a Creative Commons Attribution-Noncommercial 4.0 International License.

Introduction

Understanding the intricate interactions between cosmic phenomena and terrestrial weather patterns has long been a topic of scientific inquiry. One such interaction that has garnered significant attention is the relationship between cosmic ray (CR) and cloud cover. CRs are high-energy particles thought to originate from outside our solar system, primarily from supernovae (Polatoğlu et al., 2023). When these particles enter Earth's atmosphere, they can ionize air molecules, potentially influencing cloud formation processes (Carslaw et al., 2002). Cloud cover plays a critical role in Earth's climate system by regulating the planet's energy balance through the reflection of solar radiation and the trapping of infrared radiation (IPCC, 2021). As such, understanding the factors influencing cloud cover variability is crucial for accurate climate modeling and prediction.

CRs reaching Earth's troposphere are influenced by solar activity. Studies from about 30 years ago suggested a connection between CR and low-cloud cover, showing variations in cloud cover between solar maximum and minimum periods. This link is significant as clouds impact Earth's radiative balance and climate. Recent research also indicates correlations between CR and cloud cover on shorter timescales. However, there's debate over these connections due to methodological differences among studies. Despite this uncertainty, the potential impact of CR on climate has sparked interest in understanding how CR might affect clouds and historical climate change. The ion-aerosol clear-sky hypothesis has emerged as a prominent proposed mechanism for the CR-cloud-climate connection. Previous studies have suggested a potential link between CRs and cloud cover, with variations in CR flux potentially affecting cloud nucleation processes (Kirkby et al., 2011; Svensmark et al., 2007).

The exact nature and significance of this relationship remain contentious, with conflicting results and a need for more robust statistical analyses and observational data (Erylkin & Wolfendale, 2010; Laken et al., 2012). Machine learning (ML) techniques offer a promising avenue for exploring these complex relationships. With their ability to handle large datasets and uncover non-linear patterns, ML methods can provide new insights into the interactions between CRs and cloud cover that traditional statistical approaches might miss (Goodfellow et al., 2016). By leveraging advanced ML algorithms, we can analyze vast amounts of meteorological and cosmic ray data to identify potential correlations and causal mechanisms with greater precision.

In this study, we aim to analyze the relationship between CRs and Total Cloud Cover (TCC) globally using state-of-the-art deep learning techniques. We utilized a comprehensive dataset comprising CR flux measurements, cloud cover observations, and various meteorological parameters collected over several years. Our approach involves the application of supervised and unsupervised ML algorithms to identify patterns and test hypotheses regarding the influence of CRs on cloud formation. We begin by providing an overview of the data sources and preprocessing steps. Next, we detail the machine learning methodologies employed, including feature selection, model training, and validation. The results section presents our findings, highlighting significant correlations and the potential implications for climate science. Finally, we discuss the limitations of our study and suggest directions for future research. Through this research, we hope to contribute to the ongoing debate about the role of cosmic rays in cloud formation and, by extension, their influence on Earth's climate system. Our findings could enhance our understanding of the factors driving cloud cover variability and improve the accuracy of climate models, with broader implications for global climate predictions.

Material and Methods

Data Collection

TCC data are taken from Climate reanalysis website (<https://climatereanalyzer.org/>). Climate reanalysis describes the use of physically grounded numerical models to mimic Earth's climate throughout time, with frequent input from real-world observations (such as satellites, weather stations, radiosondes, and ocean buoys). In situations where direct observations are unavailable, reanalysis models are a crucial resource for comprehending climatic variability and change. For the most popular reanalysis products, common meteorological variables are accessible from this page. The NCAR Climate Data Guide is a good resource for users to learn more about reanalysis, including its methodology, advantages, disadvantages, and product comparisons. Advancing Reanalysis has further information about reanalysis. Copernicus C3S provided the ECMWF European Reanalysis V5 (ERA5) (0.25°x0.25°) download. Here, the data files are regridded using bilinear interpolation to

0.5°x0.5° in order to minimize access time and server burden. Gridded data products use interpolation techniques to fill in data gaps by overlaying point-based or spatially discontinuous measurements of Earth's climate (such as temperature, precipitation, wind, and sea surface temperature) onto time-registered grids. Similar to reanalysis, gridded datasets are helpful for studying climate in regions without direct observations, but where relevant information can be obtained by combining nearby input data. Numerous frequently used gridded datasets are accessible through Climate Reanalyzer. The Climate Change Institute at the University of Maine in the United States provided Climate Reanalyzer to compile this data (<https://climatechange.umaine.edu>).

As seen in Table 1, CR data was selected globally. However, Total Cloud Cover (TCC) data was selected based on different regions of the world. Cloud parameters are abbreviated as T1, T2, ..., T7. The cosmic ray data utilized in this research was sourced from the Cosmic Ray Station, a component of the University of Oulu's Sodankylä Geophysical Observatory (<https://cosmicrays oulu.fi/>).

Table 1. CR and TCC Parameters

Code	Parameters/Region	Coordinate
CR	Cosmic Ray (count/min) - World	Globally
T1	TCC (%) - Antarctica	90° S – 66.5° S, 0° E – 360° E
T2	TCC (%) - Arctic	66.5° N – 90° N, 0° E – 360° E
T3	TCC (%) - Europe	35° N – 60° N, 12° W – 30° E
T4	TCC (%) - Northern Hemisphere	0° – 90° N, 0° E – 360° E
T5	TCC (%) - Southern Hemisphere	90° S – 0° , 0° E° – 360° E
T6	TCC (%) - Atlantic Ocean	50° S – 60° N, 70° W – 10° E
T7	TCC (%) - World	90° S – 90° N, 0° E – 360° E

The station is situated in northern Finland, renowned for its minimal light pollution and conducive atmospheric conditions for cosmic ray observation. The data collection period covers the years from 1964 to 2023, capturing a comprehensive temporal scope for analysis. The Cosmic Ray Station employs a sophisticated network of neutron monitors, muon detectors, and other specialized instruments to capture CR interactions with Earth's atmosphere. These detectors are strategically positioned to mitigate environmental influences and ensure the fidelity of collected data. Continuous monitoring and data logging mechanisms are implemented to ensure uninterrupted data acquisition throughout the observation period. Quality control protocols are enforced to identify and rectify any anomalies or instrumental artifacts that may affect data integrity.

Deep Learning Methods

In this study, Long Short-Term Memory (LSTM), an advanced deep learning technique, is used to analyse the relationship between CR and TCC from 1964 to 2024. This method is particularly suited for time series data, allowing us to capture temporal dependencies and complex patterns within our dataset. LSTM networks are a type of recurrent neural network (RNN) architecture designed to effectively learn and remember long-term dependencies in sequential data. Traditional RNNs suffer from the vanishing gradient problem, where gradients diminish exponentially as they are backpropagated through time, making it difficult for the network to learn long-term dependencies. LSTMs address this issue through their unique cell structure, which includes three gates: the input gate, forget gate, and output gate. These gates regulate the flow of information, allowing the network to retain relevant information over long periods and discard unnecessary information. The core component of an LSTM is its cell state, a memory buffer that runs through the entire sequence, and is modified by the gates to store and manage long-term information. The input gate decides which information from the current input and the previous hidden state should be updated in the cell state. The forget gate determines which information in the cell state should be removed, ensuring that irrelevant data does not clutter the memory. The output gate controls what part of the cell state should be outputted and used for the current hidden state. This gated mechanism allows LSTMs to maintain a more constant error gradient, addressing the issues of both the vanishing and exploding gradient problems found in standard RNNs. These mechanisms allow the LSTM network to retain relevant information over long periods, making it powerful for time series prediction tasks. For our analysis, we implemented the LSTM model using the TensorFlow/Keras library (Graves & Graves, 2012; Hochreiter & Schmidhuber, 1997; Sherstinsky, 2020). The architecture includes multiple LSTM layers

followed by dense layers to output the final predictions for TCC based on CR data.

Before training the models, the CR and TCC data underwent several preprocessing steps:

- i) Normalization: Both CR and TCC data were normalized to ensure the models' efficient training and convergence.
- ii) Sequence Generation: The data were divided into sequences of appropriate length to train the RNN-based models.
- iii) Train-Test Split: The dataset was split into training and testing sets to evaluate the models' performance on unseen data.

By applying these advanced machine learning techniques, we aim to uncover potential correlations and causal relationships between CRs and TCC, contribute valuable insights to climate science research.

Results and Discussion

The correlation matrix shows the relationships between various variables (CR, T1, T2, T3, T4, T5, T6 and T7). The correlation coefficients range from -1 to 1, where 1 indicates a perfect positive correlation, -1 indicates a perfect negative correlation and 0 indicates no correlation. In general, the correlations in the lower right part of the matrix appear to be stronger and more positive, indicating that T4, T5, T6 and T7 are more tightly correlated with each other (Figure 1). On the other hand, the correlations between CR and other variables are generally weak and negative, suggesting that CR has no apparent relationship with these variables or there may be an inverse relationship. That is, this matrix shows that there are some strong positive relationships and weak negative relationships between certain variables. This type of analysis is useful to understand which variables act together and which are independent. A positive correlation between CR and Cloud formation is expected, whereas here it is mostly negative correlations or very weak positive correlations. T5 (Southern Hemisphere) and T7 (World) TCC values were positively correlated with CR, albeit weakly. In T1 and T2, i.e. Antarctic and Arctic polar regions, negative correlations of 0.28 and 0.19 were observed. It is understood that different climate mechanisms come into play in different regions and change these connections. One thing should not be forgotten here. The positive correlation between CR and cloud is only observed between Low Cloud Cover (LTCC) in the literature (Marsh & Svensmark, 2000). However, here we have analysed directly with TCC. For this reason, we can say that there is an important relationship between the layer of clouds and CR. In Figure 2, the Time Series graph of all parameters is drawn. The TCC values worldwide and the values in T4, T5 and T6 regions are parallel. However, changes are observed in other regions. In summary, it is difficult to see a significant correlation between CR and TCC.

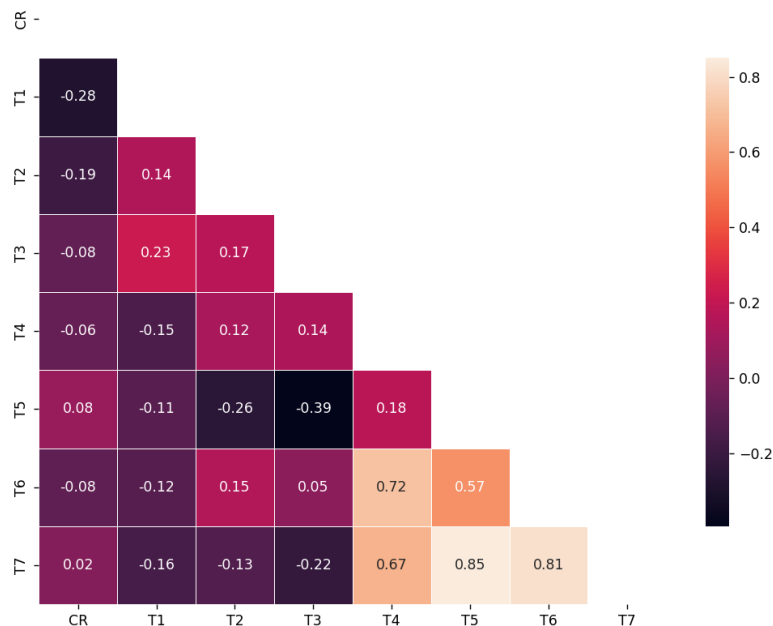


Figure 1. Correlations of CR and TCC Parameters

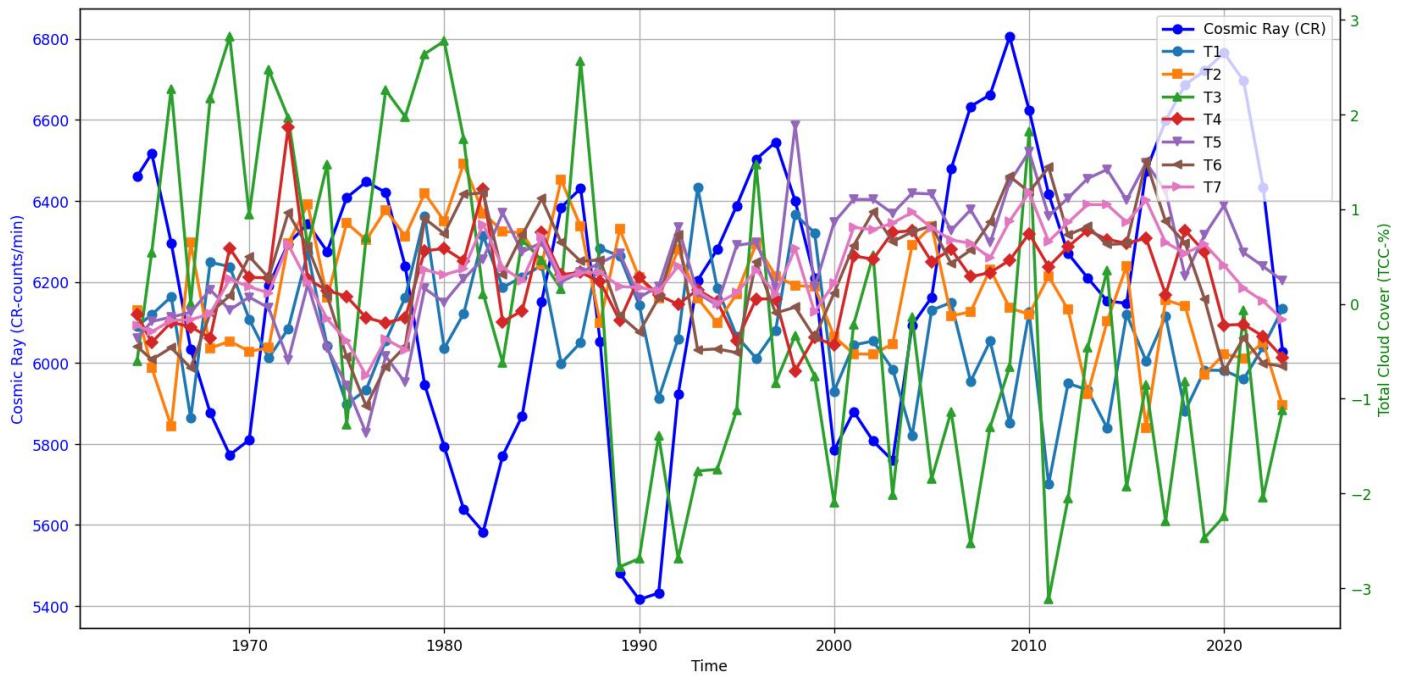


Figure 2. Time Series of CR and TCC

The predicted CR values estimated using the LSTM network do not closely follow the actual CR values (Figure 3). The predictions are quite different from the trends and changes of the actual values and follow an almost constant line. While the actual CR values show a significant seasonality or time-dependent variation, the model's predictions fail to capture these variations. This indicates that the model cannot accurately learn or represent dynamic changes and peaks. To improve the performance of the model, more data, more complex models or retraining of the model may be required. It may also be considered to add new featurettes so that the model can better capture changes. The fact that the predictions in the graph are not close to the actual CR values indicates that the current state of the model is inadequate and significant improvements are required.

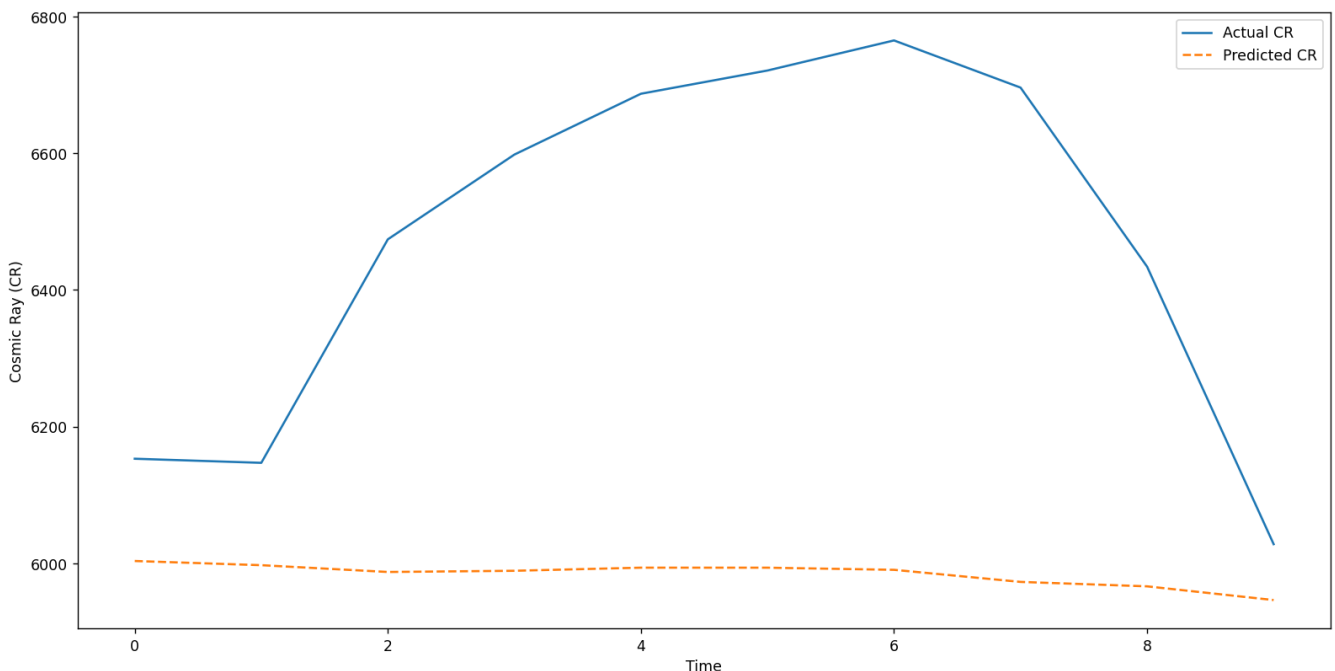


Figure 3. Actual and Predicted CR Values

Training Loss and Validation Loss decrease rapidly in the first few epochs. The term loss is used as a metric to measure the performance of the model on the training set. At the end of each epoch, this is the average loss value of the model on the training set. The term Val Loss is used as a metric to measure the performance of the model on the validation set. At the end of each epoch, this is the average loss value of the model on the validation set. This indicates that the model initially learnt the data well. As can be seen in Table 2, after Epoch 7, Val Loss reaches a minimum level and then starts to increase. This may indicate that the model is overfitting the validation set. The model fits the training set very well, but fits the validation set less well. Test Loss, Test MSE: 0.1719 indicates the performance of the model on the test set. This value is higher than the model's lowest loss on the validation set. This may indicate that the model does not generalise well to new and unseen data. The fluctuation in the validation loss during the model's training process indicates that the model is not learning consistently and is starting to overfit. This situation can usually be improved by early stopping or using more data in the training process. Also, hyperparameter adjustments can be made to improve the performance of the model. For example, parameters such as the size of the LSTM layers, learning rate, number of epochs or batch size can be adjusted. More data can be used to improve the performance of the model.

Table 2. Training Process Values

Epoch	Loss	Val Loss
0	0.3101	0.5429
1	0.2207	0.4011
2	0.1512	0.2807
3	0.1017	0.1827
4	0.0729	0.1096
5	0.0655	0.0644
6	0.0761	0.0444
7	0.0912	0.0390
8	0.0979	0.0409
9	0.0947	0.0483
10	0.0858	0.0610
11	0.0761	0.0782
12	0.0685	0.0983
13	0.0641	0.1194
14	0.0627	0.1395
15	0.0634	0.1570
16	0.0653	0.1708
17	0.0673	0.1803
18	0.0690	0.1854
19	0.0699	0.1863

Conclusion

Understanding the intricate interactions between cosmic phenomena and terrestrial weather patterns has long been a topic of scientific inquiry. One such interaction that has garnered significant attention is the relationship between CRs and cloud cover. CRs are high-energy particles thought to originate primarily from supernovae outside our solar system. When these particles enter Earth's atmosphere, they can ionize air molecules, potentially influencing cloud formation processes. Cloud cover plays a critical role in Earth's climate system by regulating the planet's energy balance through the reflection of solar radiation and the trapping of infrared radiation. As such, understanding the factors influencing cloud cover variability is crucial for accurate climate modeling and prediction. This study aims to analyze the relationship between CRs and TCC globally using state-of-the-art machine learning techniques, specifically LSTM networks. We utilized a comprehensive dataset comprising CR flux measurements, cloud cover observations, and various meteorological parameters collected over several decades. The cosmic ray data was sourced from the Cosmic Ray Station at the University of Oulu's Sodankylä Geophysical Observatory, while TCC data was obtained from the Copernicus Climate Change Service's ECMWF European Reanalysis V5 (ERA5).

Initial analyses involved constructing a correlation matrix to identify relationships between CRs and TCC across different regions, including the Antarctic, Arctic, Europe, Northern Hemisphere, Southern Hemisphere, Atlantic Ocean, and globally. The results indicated generally weak and negative correlations between CR and TCC, with a few exceptions. Notably, weak positive correlations were observed for TCC in the Southern Hemisphere and globally. Negative correlations were more pronounced in the Antarctic and Arctic regions, suggesting region-specific climate mechanisms affecting these connections. The LSTM model was employed to capture temporal dependencies and complex patterns within the dataset. Despite the sophisticated architecture of LSTM networks, the model's predictions of CR values did not closely follow the actual values, indicating a significant gap in capturing dynamic changes and peaks. This suggests that the current model configuration may require more data, additional features, or further tuning to improve accuracy. The training process revealed rapid initial learning, followed by overfitting after several epochs, as indicated by increasing validation loss. The final model's performance, measured by test MSE, suggested inadequate generalization to unseen data. These findings highlight the challenges of modeling the relationship between CRs and TCC using machine learning. The weak correlations and the model's performance indicate the complexity of these interactions and the need for more robust data and advanced modeling techniques. In these studies, it may be necessary to focus on Low-Level Cloud Cover (LCC) data to obtain more accurate results. Future research should focus on enhancing data quality, incorporating more detailed cloud cover metrics, and exploring other machine learning models to better understand the influence of cosmic rays on cloud formation and climate. This study contributes to the ongoing debate about the role of cosmic rays in climate systems, providing insights that could improve climate models and predictions:

Peer-review: Externally peer-reviewed.

Author Contributions: Concept-AP; Design-AP; Supervision-AP; Resources-AP; Data Collection and/or Processing-AP; Analysis and/or Interpretation-AP; Literature Search-AP; Writing Manuscript-AP; Critical Review-AP; Other-AP

Conflict of Interest: The author has no conflicts of interest to declare.

Financial Disclosure: The author declared that this study has received no financial support.

Hakem Değerlendirmesi: Dış bağımsız.

Yazar Katkıları: Fikir-AP; Tasarım-AP; Denetleme-AP; Kaynaklar-AP; Veri Toplanması ve/veya İşlemesi-AP; Analiz ve/veya Yorum-AP; Literatür Taraması-AP; Yazıyı Yazan-AP; Eleştirel İnceleme-AP

Çıkar Çatışması: Yazar, çıkar çatışması olmadığını beyan etmiştir.

Finansal Destek: Yazar, bu çalışma için finansal destek almadığını beyan etmiştir.

References

- Carslaw, K.S., Harrison, R.G. & Kirkby, J. (2002). Cosmic rays, clouds, and climate. *Science*, 298(5599), 1732-1737.
- Erlykin, A.D. & Wolfendale, A.W. (2010). Cosmic rays and clouds. *Journal of Atmospheric and Solar-Terrestrial Physics*, 72(5-6), 436-438.
- Goodfellow, I., Bengio, Y. & Courville, A. (2016). *Deep Learning*. MIT Press.
- Graves, A. & Graves, A. (2012). Long short-term memory. *Supervised sequence labelling with recurrent neural networks*, 37-45.
- Hochreiter, S. & Schmidhuber, J. (1997). Long short-term memory. *Neural Computation*, 9(8), 1735-1780.
- IPCC, (2021). *Climate Change 2021: The Physical Science Basis*. Contribution of Working Group I to the Sixth Assessment Report of the Intergovernmental Panel on Climate Change.
- Kirkby, J., Curtius, J., Almeida, J. & et al., (2011). Role of sulphuric acid, ammonia and galactic cosmic rays in atmospheric aerosol nucleation. *Nature*, 476(7361), 429-433.
- Laken, B.A., Kniveton, D.R. & Frogley, M.R. (2012). Cosmic rays linked to rapid mid-latitude cloud changes. *Atmospheric Chemistry and Physics*, 12(16), 7859-7867.
- Marsh, N. & Svensmark, H. (2000). Cosmic rays, clouds, and climate. *Space Science Reviews*, 94(1), 215-230.
- Polatoğlu, A., Yeşilyaprak, C., Kaya, M., Shameoni Niaei, M., & Er, H. (2023). New the Design and Measurements of the Portable Cosmic Ray Muons Detector (CRMD) for an Observatory. *Universal Journal of Physics and Application*, 17(4).
- Sherstinsky, A. (2020). Fundamentals of recurrent neural network (RNN) and long short-term memory (LSTM) network. *Physica D: Nonlinear Phenomena*, 404, 132306.

Svensmark, H., Bondo, T. & Svensmark, J. (2007). Cosmic ray decreases affect atmospheric aerosols and clouds. *Geophysical Research Letters*, 34(15).

Gama Radyasyonun Amitriptyline Hydrochloride Üzerinde Oluşturduğu Yapısal Bozuklukların Elektron Paramanyetik Rezonans (EPR) ve Simülasyon Tekniği ile İncelenmesi

Analysis of Structural Defects Caused by Gamma Radiation on Amitriptyline Hydrochloride Through Electron Paramagnetic Resonance (EPR) and Simulation Technique

Fırat AKBALIK 

Akyurt Anadolu Lisesi, Ankara, Türkiye



Öz

Bu çalışmada, depresyon semptomlarının tedavisinde sıkça kullanılan ilaç etkin maddesi Amitriptyline Hydrochloride gama radyasyonuna maruz bırakılarak oluşan paramanyetik bozukluk EPR spektroskopisi ile çalışılmıştır. Örneğin, dozimetrik malzeme olarak kullanıma uygunluğu, radikal sönüm bilgileri, mikrodalga güç değerlerinde doyum bilgileri ve doz-cevap eğrisi oda sıcaklığında araştırılmıştır. İlaç örneği farklı sıcaklık aralıklarında da ölçülmüştür. Ayrıca gama radyasyonuna maruz bırakılmayan örnekte EPS sinyali gözlenmemiştir. Spektrum simülasyonu (benzetimi) yapılarak radyasyon sonucunda oluşan radikalın spektroskopik özellikleri belirlenmiştir.

Anahtar Kelimeler: EPR, Dozimetri, Gama ışınlama

Abstract

In this study, the suitability of usage as a dosimetric material gamma-irradiated Amitriptyline Hydrochloride, which is used in treatment of symptoms of depression diseases, was studied with EPR spectroscopy. Signal fading, microwave saturation behavior and dose-response curve information were investigated at room temperature. Moreover, the drug sample was also measured at different temperature ranges, EPR signal was not detected in unirradiated samples. The spectroscopic properties of radical induced by irradiation were also determined by spectrum simulation.

Keywords: EPR, Dosimetry, Gamma irradiation

Sorumlu Yazar/Corresponding Author:

Fırat AKBALIK

E-mail: fakbalik@gmail.com

Geliş Tarihi/Received 27.02.2024

Kabul Tarihi/Accepted 15.05.2024

Yayın Tarihi/ 27.06.2024

Publication Date

Cite this article

Akbalık, F. (2024). Analysis of Structural Defects Caused by Gamma Radiation on Amitriptyline Hydrochloride Through Electron Paramagnetic Resonance (EPR) and Simulation Technique. *Journal of Anatolian Physics and Astronomy*, 3(1), 27-35.



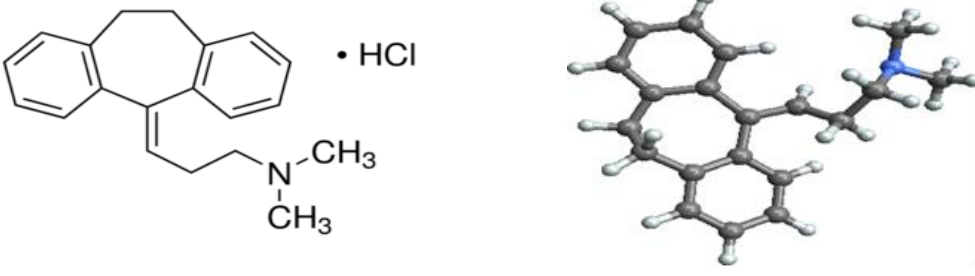
Content of this journal is licensed under a Creative Commons Attribution-Noncommercial 4.0 International License.

Giriş

Atom molekül fiziği alt alanlarından olan spektrometri ile EPR spektroskopisi çalışmalarında iyonlaştırıcı radyasyon uygulaması ile ilaç etkin maddelerinde oluşan serbest radikallerin tespiti yapılabilmekte ve tek elektronun molekül üzerine yayılımı ile ilgili bilgi edinilebilmektedir (Abbar et al., 2011; Basly & Bernard, 1997; Basly et al., 1997; Bhat & Karim, 2009; Cassella & Davis, 1985; Damian, 2003; Finčur et al., 2021; Ghasemi & Bagheri, 2020; Gibella et al., 1993; Jeon et al., 2021; Osawa et al., 2020; Polat & Korkmaz, 2006; Smyth et al., 2006).

Elektron Paramanyetik Rezonans (EPR) spektroskopisi ile ışınlanmış ilaç örnekleri üzerine yapılan çalışmaların sonuçları EPR spektroskopisinin ışınlama ile oluşan serbest radikallerin karakterizasyonunda kullanılabilecek oldukça etkili bir yöntem olduğunu açıkça göstermiştir (Basly & Bernard, 1997; Basly et al., 1997; Damian, 2003; Gibella et al., 1993; Polat & Korkmaz, 2006). Amitriptyline Hydrochloride 1950'lerin sonlarında MERCK laboratuvarlarında keşfedilmiş ve 1961'de ABD Gıda ve İlaç Dairesi (FDA) tarafından onaylanmıştır. Yine Amitriptyline Hydrochloride 2019'da Amerika Birleşik Devletleri'nde en sık reçete edilen 94. ilaç olmuştur. Amitriptyline Hydrochloride ilacının molekül formülü $C_{20}H_{23}NHCl$ dir. İlacın molekül ağırlığı 313.86 g/mol olup erime noktası $196\text{ }^{\circ}C$ 'dir. Tablo 1'de Amitriptyline Hydrochloride ilaç örneğine ait bilgiler verilmiştir.

Tablo 1. Amitriptyline Hydrochloride örneğinin kimyasal yapısı, kapalı formülü ve molekül ağırlığı

	
Amitriptyline Hydrochloride molekülünün iki boyutlu kimyasal yapısı	
Kapalı Formülü	$C_{20}H_{23}NHCl$
Molekül Ağırlığı	313.86 g/mol
Kimyasal Adı	Amitriptyline Hydrochloride

Farmakope'lerce (USP XXII, BP 1993) kabul edilen ilaç örnekleri için kullanılabilecek maksimum radyasyon dozu 25 kGy olarak seçilmiştir. Deneysel çalışmalar sürecinde, Amitriptyline Hydrochloride ilaç örneği 1, 5, 10, 15, 20 ve 25 kGy dozlarda ışınlanmış ve spektrumlar alınmıştır. Bu çalışmanın amacı, γ -ışınları ile ışınlanmış Amitriptyline Hydrochloride ilaç örneğinde oluşan serbest radikallerin spektral özelliklerinin ve oda sıcaklığında EPR incelemesi sonucu doz cevap eğrilerinin oluşturularak normal ve/veya kaza dozimetrisine örnek teşkil etmek üzere kullanılıp kullanılmayacağı durumunun belirlenmesi üzerine kurgulanmıştır. EPR ayrıca kaza dozimetrisi için de kullanılmaktadır. Kaza dozimetrisi ile ilgili açıklamalar takip eden bölümde yapılmıştır.

Kaza dozimetrisi

Kaza dozimetrisi incelendiğinde nükleer radyasyon kaynaklı kazalarda absorbe edilecek radyasyon miktarının hassas bir şekilde ölçülmesi o kazanın yaşandığı bölgedeki canlıların yaşamı açısından önemlidir. Uluslararası Atom Enerjisi Ajansı (IAEA) radyasyon kazaları sonucu maruz kalınan dozun saptanmasında biyolojik dozimetrisinin de bağımsız olarak kullanılması önerisini sunmuştur (IAEA-VIENNA, 1986). Radyasyon kazalarında kazazedelere uygulanacak tedavi yöntemleri ve tedavini önemi, olaydan hemen sonra ölçüm yapılmasına ve soğurulan dozun duyarlı bir şekilde belirlenmesine bağlıdır.

Yöntemler

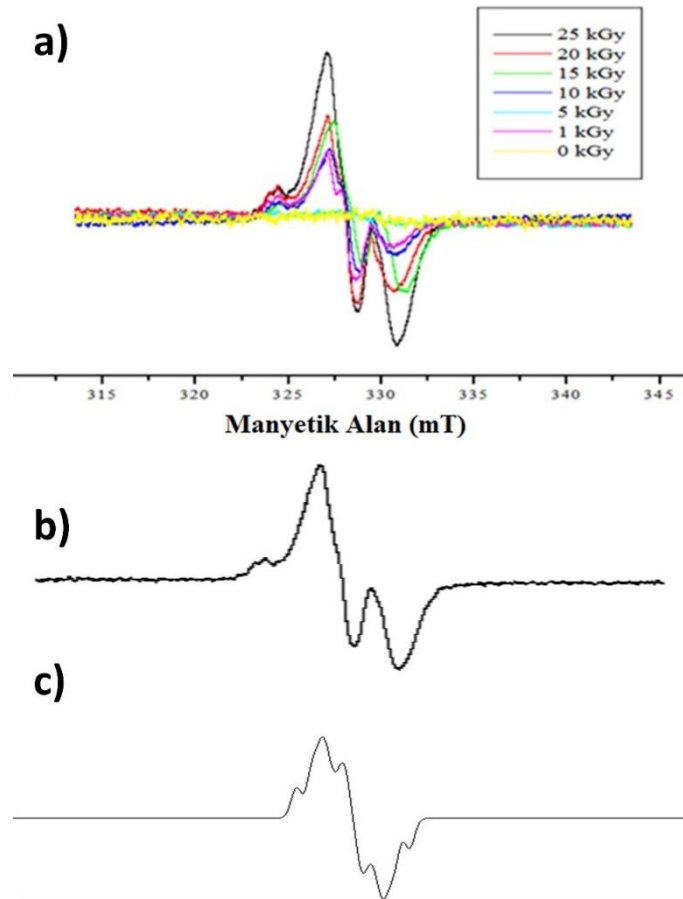
Bütün dozlardaki ışınlamalar Türkiye Atom Enerjisi Kurumu'na bağlı Kahramankazan ilçesinde bulunan Sarayköy Nükleer

Araştırma Merkezi SANAEM yeni adı ile TENMAK birimi Endüstriyel Işınlama Tesisinde aktivitesi 370.000 curie ve doz hızı 2 kGy/sa olan Kobalt-60 gama kaynağı ile gerçekleştirilmiştir. Deney sahasında gama ışınlama tesislerinde ışınlanacak ürünler numune paketleri içerisinde işlem görürler ve ürün kutularına dozimetreler konularak işlem kontrolü yapılır. Bu çalışmada kullandığımız örnekler 2 ml kapasiteli Eppendorf tüpü içinde hazırlandıktan sonra üniteye yerleştirilip ışınlandı. Hazırlanan 6 numune farklı tarihlerde sırasıyla 1 kGy, 5 kGy, 10 kGy, 15 kGy, 20 kGy ve 25 kGy dozlarda ışınlanmıştır. Depresyon semptomlarının tedavisinde sıkça kullanılan ilaç etkin maddesine ait toz haldeki numuneler üzerinde herhangi bir işlem yapılmadan sadece Eppendorf tüpü içerisine yerleştirilerek çeşitli spektrometre çalışma koşullarında EPR spektrumları kaydedilmiştir (Bruker e-scan Marka X-band EPR Spektrometresi: Merkez manyetik alan 349 mT; tarama aralığı 10 mT; mikrodalga gücü ~ 0.1 mW, mikrodalga frekans 9.8 GHz, alıcı kazancı 3.17×10^2 , modülasyon frekansı 86 kHz, modülasyon genliği 2 Gauss olarak alınmıştır). Bütün spektrum ölçümleri oda sıcaklığında kaydedilmiştir.

Bulgular

Işınlanmamış ve ışınlanmış örnekler

Bu çalışmada kullanılan Amitriptyline Hydrochloride ilaç örneği üzerinde gama ile ışınlama dışında fiziksel veya kimyasal herhangi bir işlem yapılmamıştır. Amitriptyline Hydrochloride ilaç örneği belli doz değerlerinde γ -ışınları ile ışınlanmış ve EPR spektrumları kaydedilmiştir. Işınlanmamış numunede herhangi bir EPR sinyali açığa çıkmadığı görülmüş. Düşük dozlardan yüksek dozlara doğru ışınlanmış örneklerdeki rezonans sinyallerinin doz değerine bağlı olarak gittikçe belirgin ve şiddetli hâle geldikleri Şekil 1(a)'da gösterilmiştir. Şekil 1(a) incelendiğinde g değeri yaklaşık olarak 2.0027 olan EPR spektrumu gözlenmektedir. Şekil 1(b)'de 25 kGy dozda ışınlanmış spektrum gösterilmiştir. Şekil 1(c)'de 25 kGy doz değerinde ışınlanmış örneğe ait simülasyon spektrumu gösterilmiştir.



Şekil 1 (a) Farklı dozlarda ışınlanmış Amitriptyline Hydrochloride örneğinin verilen doz değerlerinde elde edilmiş EPR spektrumları **(b)** Amitriptyline Hydrochloride örneğinin 25 kGy doz değerinde EPR spektrumu **(c)** Amitriptyline Hydrochloride örneğinin 25 kGy dozda elde edilen en yakın simülasyon spektrumu

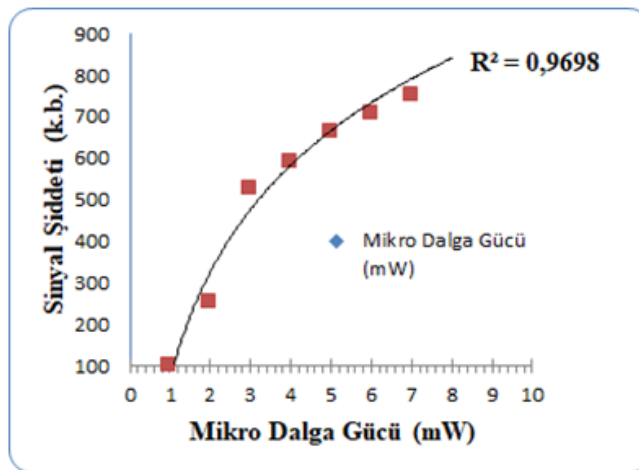
EPR sinyal şiddetinin mikrodalga gücü ile değişimi

Çalışmanın bu kesiminde 10 kGy doz değerinde ışınlanmış Amitriptyline Hydrochloride ilaç örneğinin 0.01-10 mW aralığında değişik mikrodalga güç değerlerinde EPR spektrumları kaydedilmiştir. Mikrodalga Gücü $P^{1/2}(\text{mW})^{1/2}$ ve rezonans sinyal şiddeti Tablo 2’de verilmiştir. Rezonans sinyal şiddeti hesaplanırken origin 6.0 programı kullanılmış ve program yarımı ile nümerik değerler kullanılarak üretilen spektrumda güçlü pikler belirlenerek sinyal şiddetleri hesaplanmıştır. Mikrodalga güç aralığı 0.01-1-2-4-5 ve 10 olarak seçilmiştir.

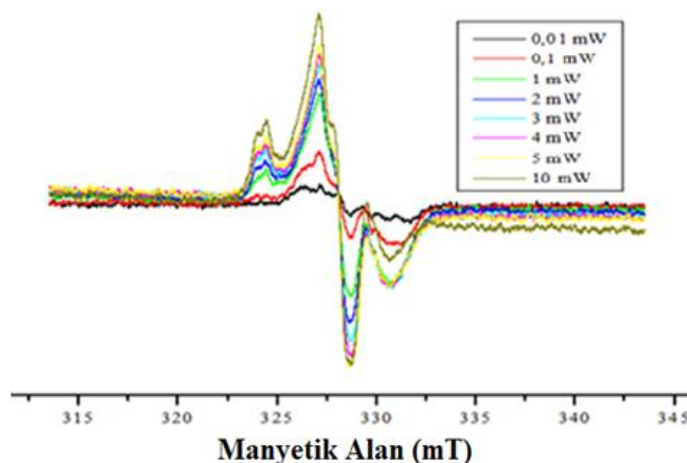
Tablo 2. Mikrodalga gücü $P^{1/2}(\text{mW})^{1/2}$ ve rezonans sinyal şiddeti

Mikrodalga gücü $P^{1/2}(\text{mW})^{1/2}$	0.01	0.1	1	2	3	4	5	10
Rezonans sinyal şiddeti	9.92	14.9	22.77	24	24.47	26.6	27.3	29

Bu bağlamda elde edilen sonuçlar Şekil 2’de gösterilmiştir. Grafik verisi origin 6.0 ile üretilmiştir. Şekil 2’de rezonans sinyaline ait grafikte kare ile gösterilen veriler deneysel sonuçları göstermektedir. Deneysel sonuçlarda en iyi uyumun en küçük değeri $R^2=0,9698$ değeriyle belirlenmiştir. Buna göre ilgili rezonans sinyal şiddetinin yaklaşık olarak 10 mW güç değerinde bile doyuma ulaşmadığı görülmektedir. Şekil 3’te ise Amitriptyline Hydrochloride örneğinin 0.01-...-10 mW aralığında değişik mikrodalga güç değerlerinde EPR spektrumları gösterilmiştir.



Şekil 2. 10 kGy dozda ışınlanmış Amitriptyline Hydrochloride ilacına ait rezonans sinyal şiddetinin mikrodalga gücü ile değişimi



Şekil 3. Amitriptyline Hydrochloride örneğinin 0.01-10 mW aralığında değişik mikrodalga güç değerlerinde EPR spektrumları

Amitriptyline Hydrochloride örneği doz-cevap eğrisi

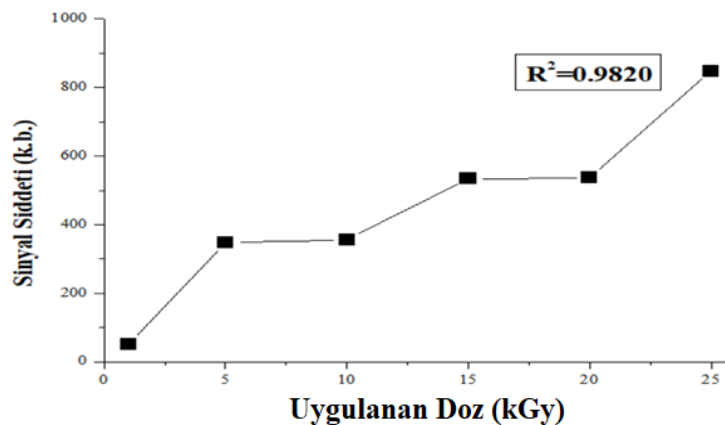
Çalışmanın bu bölümde Amitriptyline Hydrochloride ilaç örneğinin dozimetrik potansiyelinin belirlenmesi amacıyla incelemeler yapılmıştır. Rezonans sinyal şiddeti bulgularının uygulanan doza bağlı değişimlerini betimleyebilecek en uygun matematiksel fonksiyonlar grafik verilerine göre excel programı ile belirlendi. Tablo 3'te Rezonans sinyal şiddeti (I) değerleri kullanılarak denenen üç farklı matematiksel fonksiyon için hesaplanan parametre değerleri ve uyum katsayıları verilmiştir.

Tablo 3. Rezonans sinyal şiddeti (I) değerleri kullanılarak denenen üç farklı matematiksel fonksiyon için hesaplanan parametre değerleri ve uyum katsayıları

Fonksiyon	Parametreler	I
$I = a + bD$ (Doğrusal)	a	95.771
	b	27.871
	c
	r^2	0.9820
$I = a + bD + cD^2$ (Polinom)	A	96.99
	b	27.55
	c	0.0124
	r^2	0.9066
$I = aD^b$ (Üs)	A	61.56
	B	0.8018
	C
	r^2	0.9405

Bu aşamada rezonans sinyali için deneysel sonuçlara en yakın matematiksel fonksiyonlar denenmiş. Rezonans sinyal şiddeti bulgularının uygulanan doza bağlı değişimlerini betimleyebilecek en uygun matematiksel fonksiyonlar Tablo 3'te verilen matematiksel fonksiyonlar denenerek belirlendi. Örneğin doz-cevap eğrisinin doğrusal, polinom ve üs fonksiyonlarıyla uyumlu olduğu saptandı. Tablo incelendiğinde elde edilen eğrinin en iyi uyumu $I=a+bD$ doğrusal fonksiyonuyla gösterdiği belirlendi. Deneysel sonuçlarda en iyi uyumun en küçük değeri $R^2=0.9820$ değeriyle belirlendi. Burada; I örneğin EPR spektrumundan ölçülen sinyal şiddetini, D örneğe uygulanan radyasyon doz miktarını belirtmektedir.

Bir malzemenin dozimetrik olarak kullanılabilmesi için gerekli şartlardan biri de doz-cevap eğrisinin Tablo 3 verilerinde gösterilen sonuçlara bağlı olarak doğrusal olmasıdır. Amitriptyline Hydrochloride ilaç örneğinde açığa çıkan değişimin spektrumda küçük sapmalar olsa da doğrusallık gösterdiği için dozimetrik malzeme olarak kullanılabilmesi düşünülmektedir. Rezonans sinyal şiddetine göre doza bağlı değişimler Şekil 4'te gösterilmiştir. Burada siyah kare ile verilen bölgeler spektrumda açığa çıkan tepeden tepeye sinyal değerlerini göstermektedir.

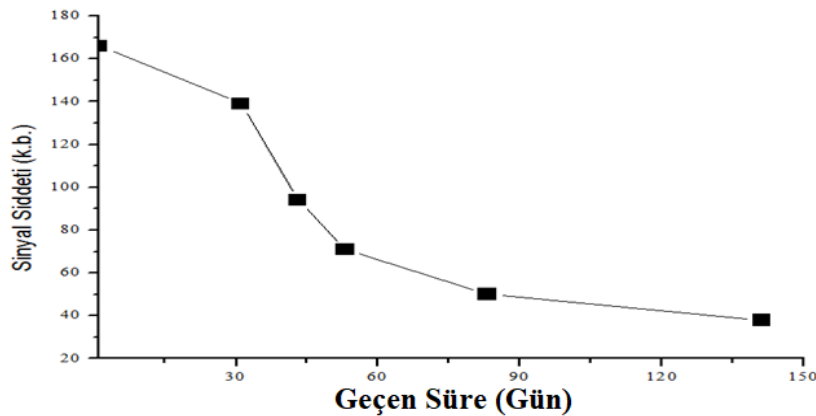


Şekil 4. 10 kGy dozda ışınlanmış Amitriptyline Hydrochloride örneği için rezonans sinyal şiddetinin uygulanan dozla değişimi

EPR sinyal şiddetinin zamanla değişimi

Çalışmanın bu bölümünde, ışınlanmış Amitriptyline Hydrochloride ilaç örneği EPR spektrumuna kaynaklık eden radikal veya radikallerin oda sıcaklığındaki kararlılıklarının belirlenmesi amaçlanmıştır. Dozimetrik amaçlı kullanılacak örnekler için radyasyonla oluşan radikal veya radikallerin oda sıcaklığında geniş zaman aralığında sönüme uğramamaları aranılan bir özelliktir. Işınlanmamış Amitriptyline Hydrochloride herhangi bir EPR sinyali vermediği göz önüne bulundurulmuş ve γ -radyasyonuna maruz bırakılan Amitriptyline Hydrochloride örneğinin ışınlamadan sonraki 150 günlük süre içerisinde izlenen tepeden tepeye sinyal şiddetinin ve spektrum alanının durumu incelenmiştir. 150 günlük süre zarfında elde edilen spektrumlarından hesap edilen rezonans sinyal şiddetinin bekleme süresine bağlı değişimi origin 6.0 programı aracılığı ile çizilmiştir. Şekil 5'te kare ile gösterilen veriler deneysel sonuçları göstermektedir. Şekilde siyah kare ile verilen bölgeler spektrumda açığa çıkan tepeden tepeye sinyal değerlerini göstermektedir. Bu süreç boyunca EPR spektrumları incelendiğinde örneğin rezonans sinyalinde geçen süreyle orantılı bir azalma gözlemlenmiş ve tepeden tepeye sinyal değerlerinde oluşan değişim incelendiğinde 30. günde sönüm kinetiğinde oluşan düşüşün % 40 olduğu, 53. günde sönüm kinetiğinin % 44 seviyesine ulaştığı ve 150. günde alınan ölçümde sönüm kinetiğinde açığa çıkan düşüşün % 86 seviyesinde gerçekleştiği görülmüştür.

Işınlanmış ilaçlarda ışınlamaya bağlı olarak elde edilen rezonans sinyalinin örneğin raf ömrü boyunca test edilebilir olması gerekmektedir (Bhat & Karim, 2009). Amitriptyline Hydrochloride örneğinde 150. günün sonunda alınan spektrumunda rezonans sinyalinin zayıfta olsa ölçülebilir olması 150. günün sonunda bile; EPR spektrometresi yöntemi kullanılarak ışınlanmış Amitriptyline Hydrochloride örneğinin ışınlanmamış olandan ayırt edilebildiğini göstermektedir. Aynı zamanda yapılan g değeri ölçümlerinde bu sürede önemli bir değişikliğin gerçekleşmediği belirlenmiştir. Şekil 5'te ışınlanmış Amitriptyline Hydrochloride örneğinde rezonans sinyal şiddetinin bekleme süresine bağlı değişimi gösterilmiştir.



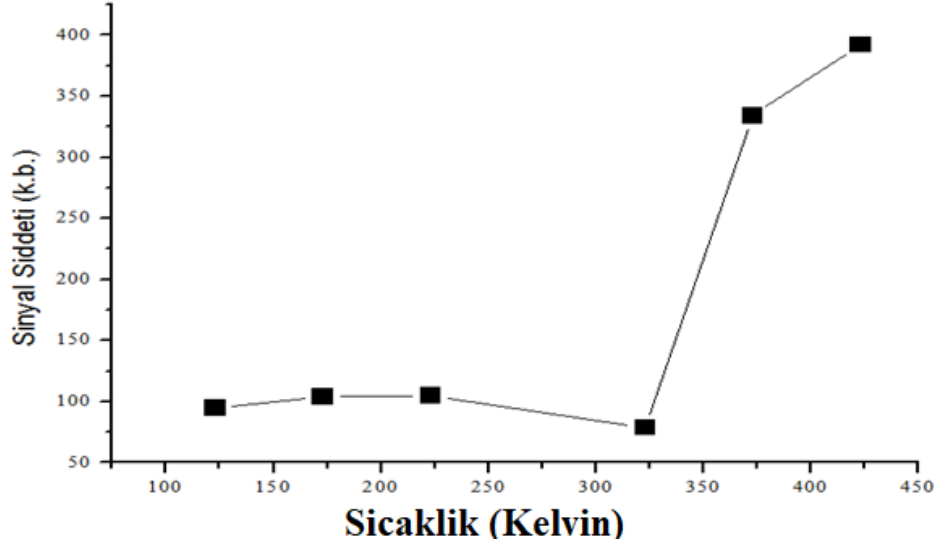
Şekil 5. 25 kGy dozda ışınlanmış Amitriptyline Hydrochloride örneğinde Rezonans sinyal şiddetinin bekleme süresine bağlı değişimi

Amitriptyline hydrochloride ilacına ait sıcaklık bulguları

15 kGy dozda ışınlanmış Amitriptyline Hydrochloride ilaç numuneleri 123-173-223-323-373-423 Kelvin aralığında 6 farklı sıcaklık değerinde spektrumları alınarak EPR ölçümleri gerçekleştirildi. Elde edilen spektrum ve sıcaklığa karşı verilen tepkiler Şekil 6'da gösterilmiştir. Işınlanmış Amitriptyline Hydrochloride ilaç örneğinde EPR spektrumunda gözlenen rezonans sinyal şiddeti değerinin sıcaklığa bağlı olarak açığa çıkardığı değişim dozimetri açısından önemlidir. Özellikle yüksek sıcaklıklarda radikal yıkımının yüksek düzeylerde olması beklenmektedir. Bu amaca yönelik olarak 15 kGy doz değerinde ışınlanmış Amitriptyline Hydrochloride örneği sıcaklığı 423 K'e ayarlanmış kavite içerisine yerleştirilmiş ve kavite sıcaklığı 50 K'lik adımlarla ilk olarak 423 K'den 373 K'e oradan 'da 323 K'e kadar düşürülmüş, buradan 223 K, 173 K ve 123 K'e kadar soğutma işlemi yapılmış ve analizler tamamlanmıştır.

123 K- 423 K aralığındaki her sıcaklık adımında Amitriptyline Hydrochloride örneğinin EPR spektrumu mikrodalga gücü ve modülasyon genliğinin sırasıyla 0.05 mW ve 1 G olduğu spektrometre çalışma koşullarında kaydedilmiştir. Bu durumun rezonans sinyal şiddeti değişimi üzerinde herhangi bir olumsuz etki yapmaması için çalışmanın bu kesiminde olabildiğince

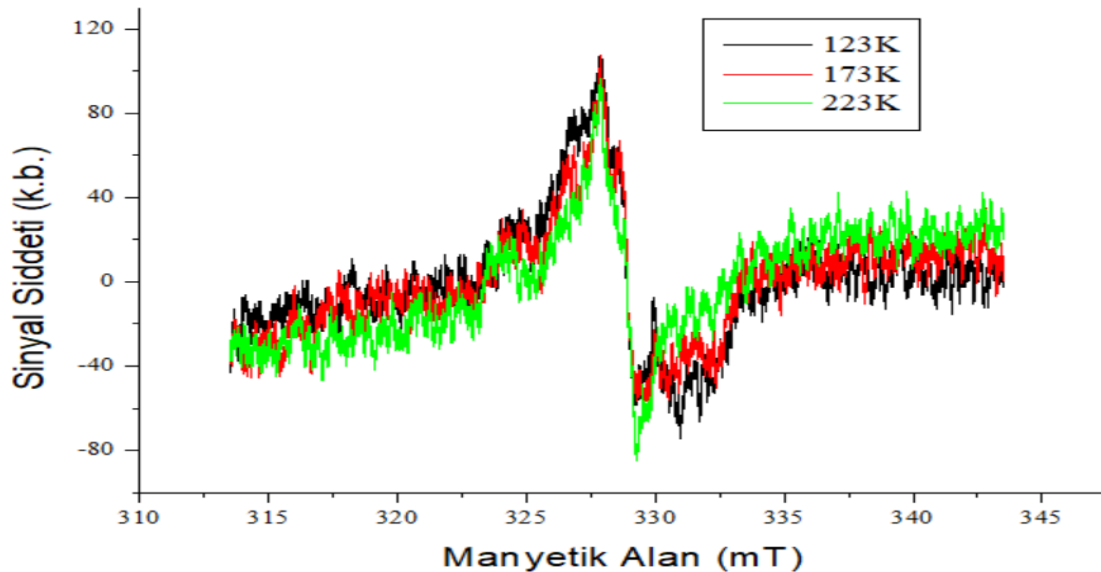
düşük mikrodalga güç değeri (0.05 mW) kullanılmıştır. 123 K-423 K aralığında 50 K artışla seçilen sıcaklıklarda kaydedilen EPR spektrumlarından rezonans sinyalinin şiddet değeri ölçülerek sıcaklıkla açığa çıkan değişimler incelenmiştir. Rezonans sinyal şiddetinin sıcaklığa bağlılığı Şekil 6'da gösterilmiştir.



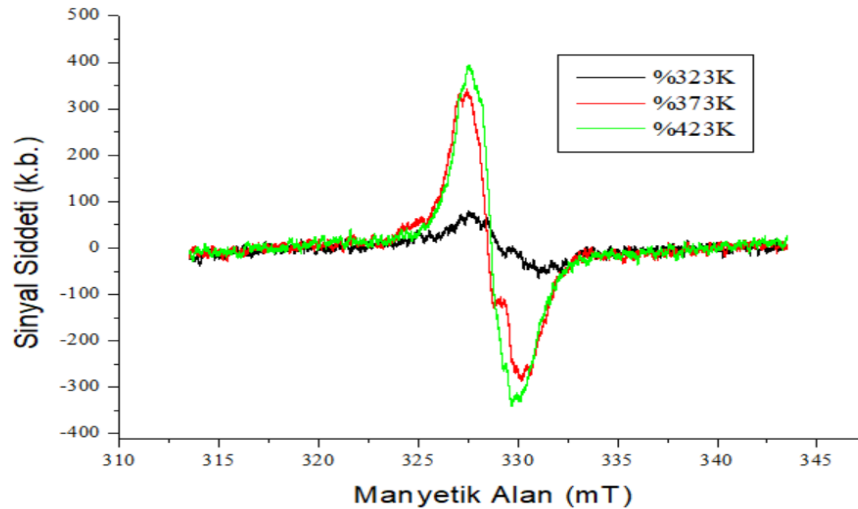
Şekil 6. 15 kGy dozda ışınlanmış Amitriptyline Hydrochloride ilacına ait sıcaklık bulguları

Sıcaklık ölçümleri çalışmasında alınan spektrumların şekillerinin birbirlerine benzediği ve şiddetlerinin değiştiği gözlemlenmiştir. Spektrumlarda meydana gelen bu değişimlerin sebebi ise ışınlama sonucu oluşan serbest elektronun düşük sıcaklıklarda hareketliliğinin azaldığı, çizgi aralığının genişlediği ve bu aralıkta şiddetin sabit kaldığı görülmüştür. Düşük sıcaklıklara ait spektrumlara ait veriler için Şekil 7 eklenmiştir. Şekil 7'de 123-173-223 K değerlerinde soğutma sonucu elde edilen spektrumlar gösterilmiştir.

Sıcaklığın artması ile radikalin hareketli hale gelip atomlar arasında gezdiği ve yüksek sıcaklıkta açığa çıkan radikal yıkımının artış gösterdiği şeklinde yorumlanmıştır. Yüksek sıcaklıklara ait spektrumlara ait veriler için Şekil 8 eklenmiştir. Şekil 8'de ise 323-373-423 K değerlerinde ısıtma sonucu elde edilen spektrumlar gösterilmiştir.



Şekil 7. Amitriptyline Hydrochloride ilacına ait soğutma sonucu elde edilen spektrumlar



Şekil 8. Amitriptyline Hydrochloride ilacına ait ısıtma sonucu elde edilen spektrumlar

Tartışma ve Sonuç

1950'lerin sonlarında MERCK'teki bilim insanları tarafından keşfedilen Amitriptyline Hydrochloride 1961'de ABD Gıda ve İlaç Dairesi (FDA) tarafından onaylanmıştır. Depresyon semptomlarının tedavisinde sıkça kullanılan ilaç 2019'da Amerika Birleşik Devletleri'nde en sık reçete edilen 94. ilaç olmuştur. Gama ışınlarıyla ışınlanmış Amitriptyline Hydrochloride ilaç örneğinin EPR spektrumu verdiği gözlenmiştir. Uygulanan doz değişimine bağlı olarak spektrumda açığa çıkan şeklin değişmediği, spektrumda sinyal gücünün arttığı belirlendi. Örneğin soğurduğu radyasyon doz miktarını tespit etmek amacıyla kütlelerine göre normalize edilmiş sinyal şiddetinin ışınlama dozuna bağlı olarak deneysel noktalardan geçen en iyi doğrunun $I=a+bD$ doğrusal fonksiyonuyla gösterdiği belirlendi. Deneysel sonuçların en iyi uyumun en küçük değeri $R^2=0.9820$ değeriyle belirlendi. Oda sıcaklığı sönüm bulguları değerlendirilerek Amitriptyline Hydrochloride spektrum simülasyon işlemleri yapıldı. Hesaplanan kuramsal spektroskopik parametre değerleri kullanılarak oluşturulan kuramsal spektrumun deneysel spektrum ile iyi uyum içerisinde olması, sonuçları değerlendirme bakımından uygun ve başarılı olduğu sonucuna varıldı.

Işınlama işlemi öncesinde Amitriptyline Hydrochloride ilaç örneğinde herhangi bir EPR sinyalinin gözlenmemesi ve doz-cevap eğrisinin geniş bir aralıkta doğrusallık göstermesi dozimetrik açıdan olumlu sonuçlardır. Sönüm spektrumlarında EPR spektrumları incelendiğinde örneğin rezonans sinyalinde geçen süreyle orantılı bir azalma gözlemlenmiş ve tepeden tepeye sinyal değerlerinde oluşan değişim origin 6.0 programı ile incelendiğinde spektrumda 30. günde sönüm kinetiğinde oluşan düşüşün % 40 olduğu, 53. günde sönüm kinetiğinin % 44 seviyesine ulaştığı ve 150. günde alınan ölçümde sönüm kinetiğinde açığa çıkan düşüşün % 86 seviyesinde gerçekleştiği görülmüştür. Bu sonuçlara göre 25 kGy dozda ışınlanan Amitriptyline Hydrochloride ilaç örneğinin dozimetrik amaçlı kullanımı durumunda, ışınlama işlemi takip eden iki gün içinde ölçümün yapılması halinde herhangi bir dezavantaj olmayacağı söylenebilir.

Hakem Değerlendirmesi: Dış bağımsız.

Çıkar Çatışması: Yazar, çıkar çatışması olmadığını beyan etmiştir.

Finansal Destek: Bu çalışma Dicle Üniversitesi Bilimsel Araştırma Projeleri Proje ID DÜBAP Fen 15-001 ile desteklenmiştir.

Teşekkür: Yazar, değerli katkılarından dolayı Prof. Dr. Şemsettin OSMANOĞLU'na teşekkür eder.

Peer-review: Externally peer-reviewed.

Conflict of Interest: The author has no conflicts of interest to declare.

Financial Disclosure: This work was supported by Dicle University Scientific Research Projects with Project ID: DÜBAP Fen 15-001.

Acknowledgment: The author would like to thank Prof. Dr. Şemsettin OSMANOĞLU for his valuable contributions.

Kaynaklar

- Abbar, J. C., Lamani, S. D., & Nandibewoor, S. T. (2011). Ruthenium (III) Catalyzed Oxidative Degradation of Amitriptyline-A Tricyclic Antidepressant Drug by Permanganate in Aqueous Acidic Medium. *Journal of Solution Chemistry*, 40(3), 502–520. <https://doi.org/10.1007/s10953-011-9655-9>
- Basly, J., & Bernard, M. (1997). Radio sterilization dosimetry by ESR spectroscopy: Ritodrine hydrochloride and comparison with other sympathomimetics. *International Journal of Pharmaceutics*, 149(1), 85–91. [https://doi.org/10.1016/s0378-5173\(96\)04855-7](https://doi.org/10.1016/s0378-5173(96)04855-7)
- Basly, J., Longy, I., & Bernard, M. (1997). ESR identification of radiosterilized pharmaceuticals: latamoxef and ceftriaxone. *International Journal of Pharmaceutics*, 158(2), 241–245. [https://doi.org/10.1016/s0378-5173\(97\)00257-3](https://doi.org/10.1016/s0378-5173(97)00257-3)
- Bhat, R., & Karim, A. A. (2009). Effect of ionizing radiation on some quality attributes of nutraceutically valued lotus seeds. *International Journal of Food Sciences and Nutrition*, 60(sup4), 9–20. <https://doi.org/10.1080/09637480802241626>
- Cassella, J. V., & Davis, M. (1985). Fear-enhanced acoustic startle is not attenuated by acute or chronic imipramine treatment in rats. *Psychopharmacology/Psychopharmacologia*, 87(3), 278–282. <https://doi.org/10.1007/bf00432707>
- Damian, G. (2003). EPR investigation of γ -irradiated anti-emetic drugs. *Talanta*, 60(5), 923–927. [https://doi.org/10.1016/s0039-9140\(03\)00153-x](https://doi.org/10.1016/s0039-9140(03)00153-x)
- Finčur, N. L., Grujić-Brojčin, M., Šćepanović, M. J., Četojević-Simin, D. D., Maletić, S. P., Stojadinović, S., & Abramović, B. F. (2021). UV-driven removal of tricyclic antidepressive drug amitriptyline using TiO₂ and TiO₂/WO₃ coatings. *Reaction Kinetics, Mechanisms and Catalysis*, 132(2), 1193–1209. <https://doi.org/10.1007/s11144-021-01936-7>
- Ghasemi, A., & Bagheri, A. (2020). Effects of alkyl chain length on synergetic interaction and micelle formation between a homologous series of n-alkyltrimethylammonium bromides and amphiphilic drug propranolol hydrochloride. *Journal of Molecular Liquids*, 298, 111948. <https://doi.org/10.1016/j.molliq.2019.111948>
- Gibella, M., Crucq, A., & Tilquin, B. (1993). Détection RPE de l'irradiation de médicaments. *Journal De Chimie Physique/Journal De Chimie Physique Et De Physico-chimie Biologique*, 90, 1041–1053. <https://doi.org/10.1051/jcp/1993901041>
- Jeon, M., Jun, B. M., Kim, S., Cho, J., Park, C. M., Choong, C. E., Jang, M., & Yoon, Y. (2021). Sonodegradation of amitriptyline and ibuprofen in the presence of Ti₃C₂T_x MXene. *Journal of Hazardous Materials Letters*, 2, 100028. <https://doi.org/10.1016/j.hazl.2021.100028>
- Osawa, R. A., Barrocas, B. T., Monteiro, O. C., Oliveira, M. C., & Florêncio, M. H. (2020). Visible light photocatalytic degradation of amitriptyline using cobalt doped titanate nanowires: Kinetics and characterization of transformation products. *Journal of Environmental Chemical Engineering*, 8(1), 103585. <https://doi.org/10.1016/j.jece.2019.103585>
- Polat, M., & Korkmaz, M. (2006). Effect of radiation on solid paracetamol: ESR identification and dosimetric features of γ -irradiated paracetamol. *Radiation Effects and Defects in Solids*, 161(1), 51–62. <https://doi.org/10.1080/10420150500467471>
- Smyth, W. F., Leslie, J. C., McClean, S., Hannigan, B., McKenna, H. P., Doherty, B., Joyce, C., & O'Kane, E. (2006). The characterisation of selected antidepressant drugs using electrospray ionisation with ion trap mass spectrometry and with quadrupole time-of-flight mass spectrometry and their determination by high-performance liquid chromatography/electrospray ionisation tandem mass spectrometry. *Rapid Communications in Mass Spectrometry/RCM. Rapid Communications in Mass Spectrometry*, 20(11), 1637–1642. <https://doi.org/10.1002/rcm.2485>.

Theoretical Structural Characterization of XIn_2Se_4 Ternary Semiconductors Wanted to be Grow Using the Bridgman/Stockbarger Technique

Bridgman/Stockbarger Tekniği Kullanılarak Büyütülen XIn_2Se_4 Üçlü Yarıiletkenlerin Teorik Yapısal Karakterizasyonu

Bekir Gürbulak 

Atatürk University, Department of Physics,
Faculty of Sciences, Erzurum, Turkey



Abstract

The importance of semiconductors paving the way for nano and optoelectronic technology has recently been increasing. But, producing them easily and having their vast application fields are most important. For that reason, the crystals have a wide application field and their characteristics which are determined are needed. Some researchers (Irie et al., 1979; Shih et al., 1986) have suggested that the crystals grown should be grown in a single ampoule and a single stage, considering the idea that it would cause selenium loss. Considering this situation, it was decided to grow XIn_2Se_4 crystal with this method. XIn_2Se_4 ($X=Cu, Mn, Al, Fe$) single crystals used in this research were grown using the Bridgman/Stockbarger method. All of the samples were freshly and gently cleaved with a razor blade from the grown ingots and no further polishing and cleaning treatments were required because of the natural mirror-like cleavage faces. The Samples were cleaved along the cleavage planes (001). In this study, single crystal growth was done in a single step. The structure of XIn_2Se_4 semiconductors was analysed theoretically using x-ray diffractometer (XRD), scanning electron microscopy (SEM), energy dispersive x-ray (EDX) and Raman spectroscopy techniques.

Keywords: Grown XIn_2Se_4 , Bridgman/Stockbarger Technique, Theoretical Structural Characterization

Öz

Nano ve optoelektronik teknolojisinin gelişmesinde yarı iletkenlerin önemi son yıllarda giderek artmaktadır. Yarıiletkenlerin kolay büyütülmesi ve geniş uygulama alanlarına sahip olması önemlidir. Kristallerin geniş bir uygulama alanına sahip olması nedeniyle, birçok özelliklerinin belirlenmesi gerekmektedir. Bazı araştırmacılar (Irie et al., 1979; Shih et al., 1986) selenyum kaybına yol açacağı düşüncesiyle büyütülen kristallerin tek ampulde ve tek aşamada büyütülmesi gerektiğini öne sürmüşlerdir. Bu durum göz önünde bulundurularak XIn_2Se_4 kristalinin bu yöntemle büyütülmesine karar verilmiştir. Bu çalışmada tek kristal büyütme tek adımda yapılmıştır. Bu araştırmada XIn_2Se_4 ($X=Cu, Mn, Al, Fe$) tek kristalleri Bridgman/Stockbarger yöntemi kullanılarak büyütülmüştür. Numunelerin tümü, büyütülen külçelerden (001) düzlemleri boyunca ayrılmıştır. Büyütülen numunelerin yüzey alanları parlak ve pürüzsüz olduğundan parlatma ve temizleme işlemlerine gerek duyulmamıştır. XIn_2Se_4 yarı iletkenlerinin yapısı, x-ışını difraktometresi (XRD), taramalı elektron mikroskobu (SEM), enerji dağılımlı x-ışını (EDX) ve Raman spektroskopisi teknikleri kullanılarak teorik olarak analiz edilmiştir.

Anahtar Kelimeler: XIn_2Se_4 Büyütme, Bridgman/Stockbarger Tekniği, Teorik Yapısal Karakterizasyon

Corresponding Author/ Sorumlu Yazar:

B. GÜRBULAK

E-mail: gurbulak@atauni.edu.tr

Received/ Geliş Tarihi 14.05.2024

Accepted/Kabul Tarihi 13.06.2024

Publication Date/ 27.06.2024

Yayın Tarihi

Cite this article

Gurbulak, B. (2024). Theoretical Structural Characterization of XIn_2Se_4 Ternary Semiconductors Wanted to be Grow Using the Bridgman/Stockbarger Technique. *Journal of Anatolian Physics and Astronomy*, 3(1), 36-43.



Content of this journal is licensed under a Creative Commons Attribution-Noncommercial 4.0 International License.

Introduction

Considering the research on the growth of single crystals, semiconductor technology continues to develop at a dizzying pace. As it is known, ternary and doped semiconductor technology lies at the basis of many applications in the world of technology and science. Most developed countries allocate serious resources for semiconductor technology and work on many different subjects. It is seen that many countries benefit significantly from renewable energy. These application areas are shaped according to certain characteristics of semiconductor compounds.

XIn_2Se_4 ($X = Cu, Mn, Al, Fe, vb.$) ternary crystals have a layered structure. The layered structures have highly anisotropic properties. Instead of three-dimensional bonding as in group II-VI, II-IV or III-V semiconductors, the molecular bonding in these crystals is first-order ionic or covalent bonds in three dimensions. This bonding mode is key to the unique properties of layered semiconductors. XIn_2Se_4 semiconductors have been widely studied for various nonlinear optical applications. Recently, there has been a renewal of interest in the magnetic properties of XIn_2Se_4 semiconductors. XIn_2Se_4 compounds have different optical and magnetic properties.

The crystallographic parameters of $CuIn_2Se_4$ crystal structure were determined. The obtained $CuIn_2Se_4$ is a black crystalline substance. Its XRD pattern (Figure 1) does not contain any lines of impurity phases; all of the lines were indexed in a tetragonal. The unit cell parameters of $CuIn_2Se_4$ were $a = 5.754 \text{ \AA}$ and $c = 11.513 \text{ \AA}$, $c/a = 2.0008 \text{ \AA}$, and $V = 382.12 \text{ \AA}^3$ (Jackson et al., 2015). Its pycnometer density was $5.319 \pm 0.007 \text{ g cm}^{-3}$. The X-ray density of 5.328 g cm^{-3} and the number of $CuIn_2Se_4$ formula units in the unit cell ($Z = 1.9995$) were calculated from the acquired data. Taking into account reflections in the XRD pattern of $CuIn_2Se_4$, the space group was established as $I4-2m$ (Krauss et al., 1997). The XRD pattern of $CuIn_2Se_4$ (see Figure 1) contains lines $00l$, wherein l is the even number not a multiple of four: $l = 2, l = 6$; in the case of a space group $I4-2d$, these lines are prohibited, while only lines $00(4l)$ are allowed. The closest analogue of $CuIn_2Se_4$ is $ZnIn_2Se_4$, which possesses the structure of unit cell parameters $a = 5.7095$ and $c = 11.449 \text{ \AA}$, $c/a = 2.0053$, $Z = 2$, and space group $I4 - 2m$ (Trah & Krämer, 1985). A comparison of the XRD patterns of $CuIn_2Se_4$ and $ZnIn_2Se_4$ revealed their good correspondence. The structures are almost equal in the compounds $CuIn_2Se_4$ and $ZnIn_2Se_4$.

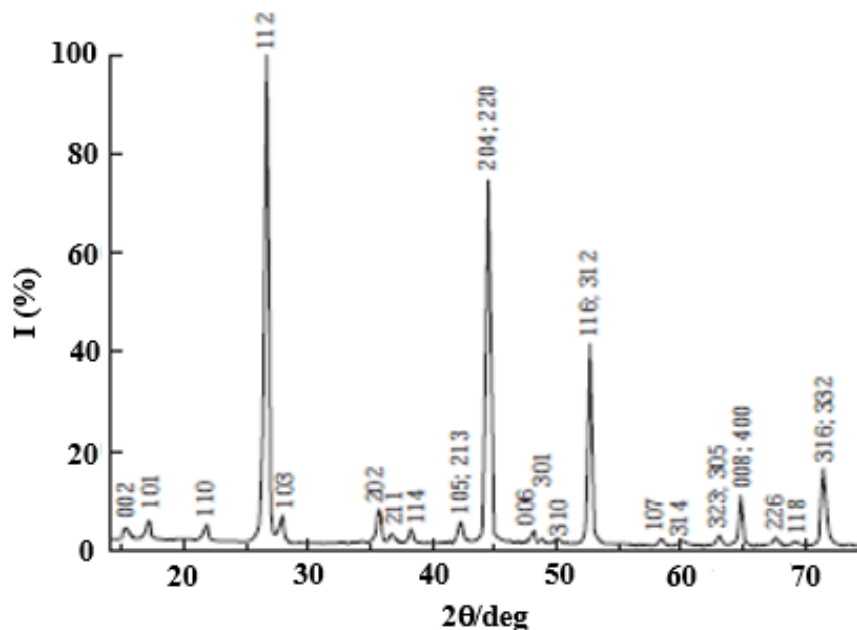


Figure. 1. XRD pattern of $CuIn_2Se_4$ (Odin et al., 2019)

The disorder in the distribution of copper and indium was also observed in the structure of $CuIn_2Se_4$: a part of copper atoms entered into the indium sublattice from its sublattice, and some indium atoms entered the copper sublattice. $CuIn_2Se_4$ is a semiconductor with $E_g = 1.08 \text{ eV}$ (Jackson et al., 2015). Therefore, the structure of $CuIn_2Se_4$ has been confirmed. The $CuIn_2Se_4$ the tetragonal unit cell parameters were determined.

The crystal structure of MnIn_2Se_4 is a rhombohedral structure with lattice parameters of $a = 4.056 \text{ \AA}$ and $c = 39.49 \text{ \AA}$ at 300 K (Döll et al., 1990). MnIn_2Se_4 semiconductor is mentioned in different literature on magnetic and optical properties. Twardowski et al. (1987) and Ramirez et al. (1994) reported a paramagnetic behaviour in MnIn_2Se_4 , whereas Quintero et al. (1997) and J. C. Woolley et al. (1994) reported a spin-glass behaviour at low temperature. The tetragonal compound the layered MnIn_2Se_4 , with rhombohedral symmetry, is synthesized by melting a stoichiometric mixture of the elements or by chemical vapour transport technique (Döll et al., 1991).

The semiconductor MnIn_2Se_4 has an energy gap of $E_g = 1,38 \text{ eV}$ (Khan et al., 1997) which is suitable for photovoltaic applications. Furthermore, the plate-like habit and easy cleavage of MnIn_2Se_4 point to a quasi-dimensional layered structure, which may influence the magnetic properties. From X-ray powder diffraction measurements (Döll et al., 1990) a rhombohedral unit cell was found for this material. From the study of the optical absorption coefficient and photoluminescence spectra of the layer semimagnetic semiconductor MnIn_2Se_4 the nature of its fundamental absorption edge is established. It is found that the lowest energy gap of this compound is allowed indirect between parabolic bands that vary from about 1,55–1,43 eV in the temperature range from 10 K to room temperature (Rincón et al. 2015). The structure of XIn_2Se_4 semiconductors was analyzed theoretically using x-ray diffractometer, scanning electron microscopy, energy dispersive x-ray and Raman spectroscopy techniques. On the other hand, its optical and electrical properties were also examined

Experimental Procedures

The structure and melting point of the XIn_2Se_4 ternary compounds have been determined. The grown XIn_2Se_4 samples are shiny and have a layered structure. There has been increased interest in the growth and characterization of derived layered compounds over the last fifteen years. XIn_2Se_4 (X= Cu, Mn, Al, Fe, etc.) single crystals were grown by the Bridgman-Stockbarger method. For the preliminary reaction, the component elements prepared in stoichiometric proportions were sealed in the growth ampoule. Grown ampoules are placed in a cage designed from kanthal DSD-Cr-Al-Fe alloy wire. It is fixed to the shaking furnace by means of connection wires made from both ends of the cage, at the appropriate distance determined, parallel to the furnace tube. Some researchers (Irie et al., 1979; Shih et al., 1986) have suggested that the crystals grown should be grown in a single ampoule and a single stage, considering the idea that it would cause selenium loss. Considering this situation, it was decided to grow XIn_2Se_4 crystal with this method.

Considering that indium would react and melt selenium as a result of thermal conductivity in the XIn_2Se_4 (X= Cu, Mn, Al, Fe, vb.) mixture, the lower and upper zone temperatures of the furnace were increased to 150 °C within 30 minutes, respectively. The reaction between In and Se was initiated by ensuring that it was above the melting temperature of indium ($\text{In}_{m.t.}$: 157 °C) and below the melting temperature of selenium ($\text{Se}_{m.t.}$: 217 °C). This will prevent the sudden increase in temperature and pressure inside the ampule. After waiting at this temperature for 50 minutes, it was increased to 217 °C within 60 minutes and kept at this temperature for 2 hours. Because the exothermic reaction between In and Se continues at 217 °C, a long time is needed to eliminate risks such as explosion or cracking of the ampule. Since selenium has a high vapour pressure between 600 °C and 950 °C, the lower and upper zone temperatures of the crystal growth furnace were increased to 500 °C within 20 hours, respectively, and waited at 500 °C for 12 hours. It is predicted that the chemical reaction between In and Se will end and the chemical reaction rate will decrease. Then, it was increased from 500 °C to 850 °C in 30 hours and remained at this temperature for 20 hours. It was then reduced to 30 °C in 48 hours. As a result of this pre-reaction process, the vapour pressure of the alloy was reduced and explosion or cracking problems in the next growth step were tried to be minimized.

Considering that the XIn_2Se_4 (X= Cu, Mn, Al, Fe, vb.) mixture will react chemically as a result of thermal conductivity and increase the vapour pressure of selenium, the lower and upper zone temperatures of the furnace were increased to 600 °C within 10 hours and the pressure risk was tried to be eliminated. This prevented the temperature and pressure inside the magnifying ampule from increasing suddenly. It was kept at this temperature for 15 hours. Because the exothermic chemical reaction between the elements In, Se, Cu, Mn, Al and Fe continues at 650 °C, a long time is needed to eliminate risks such as explosion or cracking of the ampoule. Since the selenium element has a high vapour pressure after 600 °C, it was heated to 1000 °C for 20 hours and kept for 10 hours. To ensure homogeneous distribution of In, Se, Cu, Mn and Fe elements, the

furnace was shaken by moving it up and down at an angle of approximately 45° for 5 hours. The enlargement oven is fixed at an angle of 60-70° with the horizontal.

The upper zone temperature of the crystal growth furnace was first kept constant at 1000 °C for 50 hours, then decreased to 800 °C for 70 hours, 650 °C for 50 hours, 250 °C for 40 hours and 30 C for 10 hours. The lower zone temperature of the furnace was reduced to 800 °C in 50 hours, to 650 °C in 70 hours, to 250 °C in 40 hours, to 100 °C in 10 hours and to 30 °C in 10 hours, and the furnace was turned off. Thus, at the same time and using the same growth temperature program, the growth process of XIn_2Se_4 ternary semiconductor crystals was completed in approximately 5 days and 14 days including the reaction. At the end of the growing process, it was removed from the oven. The ampoules were cut with the help of a suitable cutter to ensure that the nugget crystal did not suffer any hardness or deformation. The ingot must be stored in a very clean environment to avoid chemical contamination of the samples (Gürbulak et al. 2021; Gürbulak, 1997; Bodnar et al., 2010; Dotzel & Schafer, 1976).

Growth and Characterization

The first important step in obtaining high quality crystal is the purity of the main materials in the structure. These elements were weighed stoichiometrically to an accuracy of 0.001 mg. The total mass of the ingredients is approximately 100 grams. The main criteria for this selection were, first of all, the cost of a single operation, sufficient need and minimal loss of material in the form of cracking of the ampoule. The elements to be used in the growth (Cu, Mn, Al, Fe, In and Se etc.) were used in high purity (99.999%) pieces with a particle size of approximately 200 mesh. The elements were weighed and loaded into a thick-walled quartz ampoule. Quartz ampoules are sealed under pressure of approximately 10^{-6} Torr. For this purpose, XIn_2Se_4 (X=Cu, Mn, Al, Fe) etc.) semiconductor was grown with the Bridgman/Stockbarger technique developed in our current crystal growth laboratory.

XIn_2Se_4 (X=Cu, Mn, Al, Fe, etc.) belongs to the family of layered ternary semiconductors known as chalcopyrite compounds. These materials have drawn significant interest due to their promising optoelectronic and photovoltaic properties. To provide a detailed theoretical understanding of the structural characterization of XIn_2Se_4 , we'll delve into several key aspects. The crystal structure of XIn_2Se_4 is based on a tetragonal, rhombohedral and hexagonal unit cell. It belongs to the space group I-42d. The lattice parameters vary slightly depending on the specific element X (Cu, Mn, Al, Fe). The unit cell typically contains multiple layers stacked along the c-axis. The crystal structure of XIn_2Se_4 consists of layers of covalently bonded Se atoms sandwiched between layers of metal cations. This layered structure contributes to the anisotropic properties of the material.

The bonding in XIn_2Se_4 is predominantly covalent between Se atoms and metal cations, while there also exist weaker van der Waals forces between adjacent layers. The covalent bonding within the layers provides stability to the crystal structure, while the weaker interlayer interactions allow for easy cleavage along certain crystallographic planes.

The presence of defects, such as vacancies or interstitials, can influence the electronic and optical properties of XIn_2Se_4 . Additionally, intentional doping with different elements (Cu, Mn, Al, Fe) can tailor the material's properties for specific applications by altering its electronic band structure and conductivity. Experimental techniques such as X-ray diffraction (XRD), scanning electron microscopy (SEM), transmission electron microscopy (TEM), and energy-dispersive X-ray spectroscopy (EDS) are commonly used to characterize the crystal structure, morphology and elemental composition of XIn_2Se_4 samples.

Density functional theory calculations can provide insights into the electronic structure, band gap, and other properties of XIn_2Se_4 . Computational simulations can complement experimental observations and aid in the understanding of its behaviour under different conditions. Understanding the structural characterization of XIn_2Se_4 is crucial for optimizing its properties for applications in solar cells, photodetectors, and other optoelectronic devices. Both experimental and theoretical approaches play key roles in advancing our knowledge of this material's properties and potential applications.

Growth and structural characterizations of single crystals like $CuIn_2Se_4$, $MnIn_2Se_4$, $AlIn_2Se_4$ and $FeIn_2Se_4$ typically involve several steps and techniques. Here's a general overview of the process:

- i. Crystal growth technique: Single crystals are often grown using methods such as the Bridgman method, chemical vapour transport (CVT), or the flux method. Each method has its advantages and is chosen based on factors like material properties and desired crystal quality.
- ii. Material preparation: High-purity starting materials are required for crystal growth. These materials are weighed according to the stoichiometric ratio of the compound and then mixed thoroughly.
- iii. Crystal growth: The chosen method for crystal growth is employed. In the Bridgman-Stockbarger method, for example, the mixed materials are loaded into a crucible and melted at high temperatures. Then, a nucleus crystal is slowly pulled from the melt, allowing the desired compound to crystallize around it.
- iv. Characterization techniques:
 - X-ray Diffraction (XRD): XRD is used to determine the crystal structure, phase purity, and orientation of the grown crystals. It provides information about lattice parameters, crystal symmetry, and crystal quality.
 - Scanning Electron Microscopy (SEM): SEM is used to study the surface morphology and microstructure of the crystals. It provides high-resolution images that can reveal details about defects, grain boundaries, and surface features.
 - Energy-Dispersive X-ray Spectroscopy (EDS): EDS is often coupled with SEM to provide elemental analysis of the crystals. It helps confirm the stoichiometry and composition of the grown crystals.
 - Raman Spectroscopy: Raman spectroscopy is used to study vibrational modes and lattice dynamics in the crystals. It can provide information about crystal quality, defects, and phonon modes.
 - Optical Characterization: Techniques like UV-Vis spectroscopy and photoluminescence spectroscopy are used to study the optical properties of the crystals, including bandgap energy, absorption spectra, and emission spectra.
 - Electrical Characterization: Electrical measurements such as Hall effect measurements, resistivity measurements, and conductivity measurements are performed to understand the electrical properties of the crystals, including carrier concentration, mobility, and conductivity type.
- v. Data analysis: The data obtained from various characterization techniques are analyzed to understand the crystal structure, composition, morphology, and properties of the grown crystals. This analysis often involves comparing experimental data with theoretical models and known reference materials.

In conclusion; by employing these techniques and methods, researchers can gain valuable insights into the growth and structural characteristics of single crystals like CuIn_2Se_4 , MnIn_2Se_4 , AlIn_2Se_4 and FeIn_2Se_4 , which are important for various applications such as photovoltaics, thermoelectric, and spintronics

Results and Discussions

XIn_2Se_4 (X= Cu, Mn, Al, Fe, etc.) single crystals were grown by the Bridgman-Stockbarger method. The structure and melting point of the XIn_2Se_4 ternary compounds have been determined. The grown XIn_2Se_4 samples are shiny and have a layered structure. In recent years, interest in the growth and characterization of derived layered compounds has increased. FeIn_2Se_4 , MnIn_2Se_4 and CuIn_2Se_4 semiconductor compounds belong to the II-III₂-VI₄ semiconductor family. Semiconductor samples crystallize in rhombic, hexagonal and tetragonal crystallographic structures, respectively.

The choice of growth technique for a given sample depends on many factors. In summary, these factors are;

- Chemical reactivity components of the compound and elements,
- Decomposition vapour pressure of the compound at the growth temperature,
- The melting point of the elements and the melting point of the compound,
- It depends on the presence or absence of phase transformations.

The general procedure for cleaning semiconductor compound ampoules is as follows.

- The magnification ampoules should be cleaned with diluted HNO_3 for approximately four hours to remove metallic contamination on the surface.

- Then it should be rinsed repeatedly with deionized water.
- The inner surface of the magnifying ampoule should be washed with liquid gel for 30 hours to remove dust particles and oils.
- It should be rinsed again with deionized water.
- The inner and outer surfaces of the growth ampoule should be etched with HF (45% diluted) for 6 minutes to further remove residual contaminations.
- The magnification ampoule should be rinsed once again with deionized water.
- Then it should be washed with acetone.
- The magnification ampoule should be washed ultrasonically in deionized water.
- In the growth oven, the ampoule should be baked at 750 °C for 30 hours.
- Plastic gloves should be worn to prevent contamination of the growth ampoules.

As a result, the following procedures must be applied to grow quality single crystals.

- The purity of the elements used in the compound must be approximately 6N.
- A very precise scale must be used to weigh the elements.
- Plastic holders should be used for weighing chemical elements and transferring them via ampoules.
- It should be known whether chemical elements are harmful to the researcher.
- It should be known whether chemical elements react with the ampoules.
- The ampoules used in the growth process must be clean.
- Gloves must be used when transferring chemical elements to ampoules.
- Growth ampoules should be prepared according to the layered or chain structure of the semiconductor sample.
- Growth ampoules should be coated with carbon.
- Pre-reaction should be done to ensure homogeneity of the compound.
- The optical and electrical properties of the grown compound must be known very well.
- If the compound has a phase, the vapour pressure and melting point of the elements must be known.
- The growth laboratory should be clean and noiseless.
- The growth laboratory should be located away from vibration.
- Since the semiconductor sample growth process takes 5-25 days, an uninterruptible power supply must be used (Gürbulak et al., 1999).

As a result, it is important to grow XIn_2Se_4 (X=Cu, Mn, Al, Fe) semiconductors using the Bridgman-Stockbarger method. While enlarging these samples to be enlarged;

- ✓ Factors affecting the selection of the growth technique,
- ✓ General procedures for cleaning growth ampoules,
- ✓ Recommended procedures for growing single crystals, must be taken into consideration.

Conclusions

Both experimental and theoretical approaches play a key role in gaining scientific knowledge about the structural properties and potential applications of this material. Understanding the theoretical structural characterization of layered XIn_2Se_4 (X=Cu, Mn, Al, Fe) is crucial for optimizing its properties for applications in solar cells, photodetectors, and other optoelectronic devices. On the other hand; both experimental and theoretical approaches play a key role in gaining scientific knowledge about the structural properties and potential applications of this material.

Peer-review: Externally peer-reviewed.

Conflict of Interest: The author has no conflicts of interest to declare.

Financial Disclosure: This work "FYL-2023-10176, Project ID: 10176 Structural Characterization of $X^m\text{In}_2\text{Se}_4$ (X^m : Cu, Mn, Fe, Ni, etc.) Ternary Semiconductors Grown by Bridgman/Stockbarger Technique," was supported by Atatürk University BAP (Scientific Research Projects).

Hakem Değerlendirmesi: Dış bağımsız.

Çıkar Çatışması: Yazar, çıkar çatışması olmadığını beyan etmiştir.

Finansal Destek: Bu çalışma "FYL-2023-10176, Proje ID: 10176 Bridgman/Stockbarger Tekniği ile Yetiştirilen $\text{XIIIIn}_2\text{Se}_4$ (XII: Cu, Mn, Fe, Ni, vb.) Üçlü Yarı İletkenlerin Yapısal Karakterizasyonu" Atatürk Üniversitesi BAP (Bilimsel Araştırma Projeleri) tarafından desteklenmiştir.

References

- Bodnar, I. V., Viktorov, I. A., & Pavlyukovets, S. A. (2010). Growth, structure, and thermal expansion anisotropy of FeIn_2Se_4 single crystals. *Inorganic Materials*, 46, 604-608.
- Döll, G., Anghel, A., Baumann, J. R., Bucher, E., Ramirez, A. P., & Range, K. J. (1991). Structural and magnetic properties of the ternary manganese compound semiconductors MnAl_2Te_4 , MnIn_2Te_4 , and MnIn_2Se_4 . *Physica Status Solidi (A)*, 126(1), 237-244.
- Döll, G., Lux-Steiner, M. C., Kloc, C., Baumann, J. R., & Bucher, E. (1990). Chemical vapour transport and structural characterization of layered MnIn_2Se_4 single crystals. *Journal of crystal growth*, 104(3), 593-600.
- Dotzel, P., & Schafer, H. (1976). Schon "Combined infrared and raman study of the optical phonons of defect chalcopyrite single crystals". *Z. Anorg. Allg. Chem*, 426, 260.
- Gürbulak, B. (1997). İkili (InSe : Er, GaSe, GaSe: Gd) ve Üçlü (TlGaSe_2 , TlGaSe_2 : Gd) Tek Kristallerinin Büyütülmesi Soğurma ve Elektriksel Özelliklerinin İncelenmesi. Atatürk Üniversitesi Fen Bilimleri Enstitüsü, Doktora Tezi, Erzurum.
- Gürbulak, B., Ateş, A., Doğan, S., Coşkun, C., Yıldırım, M. & Yoğurtçu, Y. K. (1999). *Bulletin of Pure and Applied Sciences*. 18(1), 33-40.
- Gürbulak, B., Duman, K. A., & Dumanlı, M. K. (2021). Bridgman/Stockbarger Tekniğiyle Büyütülen $\text{XIIIIn}_2\text{Se}_4$ Üçlü Yarıiletkenlerin Yapısal Karakterizasyonu. *Journal of Anatolian Physics and Astronomy*, 1(2), 77-85.
- Irie, T., Endo, S., & Kimura, S. (1979). Electrical properties of p-and n-type CuInSe_2 single crystals. *Japanese Journal of Applied Physics*, 18(7), 1303.
- Jackson, P., Hariskos, D., Wuerz, R., Kiowski, O., Bauer, A., Friedlmeier, T. M., & Powalla, M. (2015). Properties of Cu (In, Ga) Se_2 solar cells with new record efficiencies up to 21.7%. *physica status solidi (RRL)–Rapid Research Letters*, 9(1), 28-31.
- Khan, A., Diaz, J., Sagredo, V., & Vargas, R. (1997). Chemical vapor transport and optical, magnetic and structural characterization of platelete-type $\text{MnxHo}_{1-x}\text{InSe}_4$ single crystals. *Journal of crystal growth*, 174(1-4), 783-789.
- Krauss, G., Krämer, V., Eifler, A., Riede, V., & Wenger, S. (1997). Growth and characterization of CdAl_2S_4 and CdAl_2Se_4 single crystals. *Crystal Research and Technology*, 32(2), 223-227.
- Odin, I. N., Chukichev, M. V., Vasiliev, A. V., Gapanovich, M. V., & Novikov, G. F. (2019). Crystallographic, magnetic and luminescence characteristics of CuIn_2Se_4 with a cadmium thioaluminate structure and $\text{Cu}(\text{In}_{1-x}\text{Ga}_x)_2\text{Se}_4$ solid solutions ($0 < x \leq 0.3$). *Mendeleev Communications*, 29(3), 276-278.
- Quintero, M., Morocoima, M., Rivero, A., Bocaranda, P., & Woolley, J. C. (1997). $\text{Cu}_2(1-z)\text{MnzIn}_2\text{Se}_4$ alloys; phase diagram and effects of Mn ordering on magnetic behaviour. *Journal of Physics and Chemistry of Solids*, 58(3), 491-496.
- Ramirez, A. P. (1994). Strongly geometrically frustrated magnets. *Annual Review of Materials Science*, 24(1), 453-480.
- Rincón, C., Torres, T. E., Sagredo, V., Jiménez-Sandoval, S. J., & Mares-Jacinto, E. (2015). The fundamental absorption edge in MnIn_2Se_4 layer semi-magnetic semiconductor. *Physica B: Condensed Matter*, 477, 123-128.
- Shih, I., Champness, C. H., & Shahidi, A. V. (1986). Growth by directional freezing of CuInSe_2 and diffused homojunctions in bulk material. *Solar cells*, 16, 27-41.

Trah, H. P., & Krämer, V. (1985). Crystal structure of zinc indium selenide, $ZnIn_2Se_4$. *Zeitschrift für Kristallographie*, 173(3-4), 199-203.

Twardowski, A., Swagten, H. J. M., De Jonge, W. J. M., & Demianiuk, M. (1987). Magnetic behavior of the diluted magnetic semiconductor $Zn_{1-x}Mn_xSe$. *Physical Review B*, 36(13), 7013.

Woolley, J. C., Bass, S., Lamarche, A. M., & Lamarche, G. (1994). Magnetic susceptibility and exchange interaction parameters for some $Mn_{III}V_{IV}$ compounds. *Journal of magnetism and magnetic materials*, 131(1-2), 199-209.